

Geometrical structure and the electron transport properties of monolayer and bilayer silicene near the semimetal-insulator transition point in tight-binding model

Chen-Huan Wu *

Key Laboratory of Atomic & Molecular Physics and Functional Materials of Gansu Province, College of Physics and Electronic Engineering, Northwest Normal University, Lanzhou 730070, China

May 2, 2018

We investigate the electron properties of the monolayer and bilayer silicene which is the honeycomb lattice consist of silicon atoms, including the optical conductivity and charged impurity scattering, due to the quasiparticle Dirac-like behaviors near the K-point of silicene. The spin, valley, sublattice degrees of freedom are taken into consider in the multi-band tight-binding model. In momentum space, the scattering matrix which connects the two bare (without interaction) Green's functions in the quasiparticle momentum transport process, could be momentum-independent for the single impurity configuration, which is similar to the case with small Coulomb coupling in the low-energy Dirac semimetallic system. While in the zero-frequency limit, or the frequency-independent case in the strong Coulomb coupling regime, the static polarization can be obtained by the random-phase-approximation, and it's important for the determination of the screened Coulomb scattering by the charge impurity. The antiferromagnetic order in the silicene is Hubbard-U-dependent, unlike the square lattice which with the antiferromagnetic ground state, and provides the premise of the phase transition from the nonmagnetic semimetal phase to the insulator one. We found that in the absence of electric field, the critical value of the phase transition from semimetal to insulator is 9 eV for the clear monolayer silicene, and is 12 eV for the 2nd AA-stacked bilayer silicene or the dirty monolayer silicene whcih with impurity strength 4 eV. While the behaviors of 1st AA-stacked bilayer silicene is found similar to the monolayer one. The in-plane optical conductivity also shows the same results.

1 Introduction

Silicene, a topological insulator (TI) together with it's bilayer form or nanoribbon form which have been synthesized experimentally[1], has very remarkable properties like the graphene[2], and its atom structure was shown in Fig.1(a), and the hexagonal Brillouin zone (BZ) was shown in Fig.1(b) with its zigzag edge and armchair edge in two directions. The low-energy dynamics of silicene can be well described by the Dirac-theory. The silicene is also a $3p$ -orbital-based materials with the noncoplanar low-buckled (with a buckle about 0.46 \AA due to the hybridization between the sp^2 -binding and the sp^3 -binding (which the bond angle is 109.47°) and that can be verified by thr Raman spectrum as shown in the Fig.1(e) which with the intense peak at 578 cm^{-1} larger than the planar one and the sp^3 -binding one [3], and thus

*chenhuanwu1@gmail.com

approximately forms two surface-effect like the thin ferromagnet matter) lattice structure. The bulked structure not only breaks the lattice inversion symmetry, but also induce a exchange splitting between the upper atoms plane and the lower atom plane and thus forms a emission geometry which allows the optical interband transitions, which for the graphene can happen only upon a FM substrate[4]. The FM or AFM order can be formed in monolayer silicene by the magnetic proximity effect that applying both the perpendicular electric field and in-plane FM or AFM field. Silicene has much stronger intrinsic spin-orbit coupling (SOC) and stronger interlayer interaction compared to the graphene due to its heavier atom mass and low-bulked structure, respectively. The bilayer silicene holds both the topological and SC properties by the, e.g., AFM $d_1 + id_2$ -pairing, rather than the s -wave one. There are four kinds of the stacking way for the bilayer silicene with different overlap and buckled-toward directions, but all with a Bravais lattice unit cell containing four silicon atoms. Among these four kinds of bilayer silicene, the AB-bt one has been found as the most stable one[5] and thus naturely has the lowest formation energy as 0.586 eV. In the Ref.[5], the AB-bt bilayer silicene has been found that with largest overlap between the lowest conduction band and the highest valence band as 300 meV, which shows that it's in a metal phase and thus with a extended Fermi surface. In this paper we only focus on the two kinds of AA-stacked bilayer silicene (see Fig.1(d) for the side view) which has a higher formation energy but lower cohesive energy compared to the AB-stacked (Bernal) one, and we only consider the vertical hopping (NN) here unlike for the AB-stacked one.

2 Geometrical structure of the layered silicene

We consider the nearest-neighbor (NN) hopping t and the next-nearest-neighbor (NNN) hopping t' of silicene in this section where we imagine a isotropic honeycomb lattice with particle-hole symmetry (PHS) (see the Schematic diagram in Fig.1) and ignore the diagonal hopping in hexagonal lattice which is qualitatively unimportant. Then the transfer Hamiltonian H_t can be written as

$$\begin{aligned}
H_t &= \begin{pmatrix} H_{AB'} & H_{AA'} \\ H_{A'A} & H_{A'B} \end{pmatrix}, \\
H_{AB'} &= \epsilon_A + t'_{AB'} \left(4 \cos \frac{\sqrt{3}k_x a}{2} \cos \frac{k_y a}{2} + 2 \cos k_y a \right), \\
H_{AA'} &= H_{A'A}^* = t_{AA'} \left[\exp\left(i \frac{\sqrt{3}k_x a}{3}\right) + \exp\left(i \left(-\frac{\sqrt{3}}{6}k_x a + \frac{k_y a}{2}\right)\right) + \exp\left(i \left(-\frac{\sqrt{3}k_x a}{6} - \frac{k_y a}{2}\right)\right) \right], \\
H_{A'B} &= \epsilon_{A'} + t'_{A'B} \left(4 \cos \frac{\sqrt{3}k_x a}{2} \cos \frac{k_y a}{2} + 2 \cos k_y a \right),
\end{aligned} \tag{1}$$

where ϵ_A is the on-site energy and $a = 3.86 \text{ \AA}$ is the lattice constant. The upper and lower band energies are

$$\begin{aligned}
E_+(k_x, k_y) &= t \cos \frac{\sqrt{3}k_x a}{3} + 2t \cos \frac{\sqrt{3}k_x a}{6} \cos \frac{k_y a}{2} + 4t' \cos \frac{\sqrt{3}k_x a}{2} \cos \frac{k_y a}{2} + 2t' \cos k_y a, \\
E_-(k_x, k_y) &= t \cos \frac{\sqrt{3}k_x a}{3} - t \cos \frac{\sqrt{3}k_x a}{6} \cos \frac{k_y a}{2},
\end{aligned} \tag{2}$$

The plot of upper band energy is shown in the upper panel of Fig.2. It's clearly that the lower and upper band energies are split by t and t' , and indeed it's origin from the hybridization of eigenstates with plane-wave states. Thus we can obtain that the bands width and the flatness are related to the t and t' . Then the on-site energy within the single-particle picture can be

obtained as[6]

$$\begin{aligned}
\varepsilon_k^2 = & 3t^2 + 2t^2 \left[\cos\left(-\frac{\sqrt{3}}{2}k_x a + \frac{1}{2}k_y a\right) + \cos\left(-\frac{\sqrt{3}}{2}k_x a - \frac{1}{2}k_y a\right) + \cos\left(\frac{\sqrt{3}k_y a}{3}\right) \right] \\
& + 6t'^2 + 2t'^2 \left[\cos(k_y a) + \cos(-k_y a) + \cos\left(\frac{\sqrt{3}}{2}k_x a - \frac{k_y a}{2}\right) + \cos\left(\frac{\sqrt{3}}{2}k_x a + \frac{k_y a}{2}\right) \right. \\
& \left. + \cos\left(-\frac{\sqrt{3}}{2}k_x a - \frac{k_y a}{2}\right) + \cos\left(-\frac{\sqrt{3}}{2}k_x a + \frac{k_y a}{2}\right) \right] \\
& + 2t'^2 \left[\cos(\sqrt{3}k_x a) + \cos(-\sqrt{3}k_x a) + \cos\left(-\frac{\sqrt{3}}{2}k_x a + \frac{3k_y a}{2}\right) + \cos\left(-\frac{\sqrt{3}}{2}k_x a + \frac{3k_y a}{2}\right) \right. \\
& \left. + \cos\left(\frac{\sqrt{3}}{2}k_x a - \frac{3k_y a}{2}\right) + \cos\left(\frac{\sqrt{3}}{2}k_x a - \frac{3k_y a}{2}\right) \right],
\end{aligned} \tag{3}$$

where the ε_k also describe the dispersion of such hopping configuration which contain nine different hopping directions. The charts of E_+ and ε_k^2 with different t' and E_- are shown in the top and bottom panel of Fig.2, respectively. We can see that the spatial fluctuations are enhanced with the increasing t' . That means the system is become less stable for increasing t' and the SDW is reduced in the mean time. Base on the process which taking account the above band energies E_{\pm} , we can obtain the two-band model with the two energy bands which intersect the Fermi surface. Note that here we ignore the bulking distance for simplify the calculation, the tight-binding results considering the bulking distance are presented in the following.

While for the pairing scattering process which mentioned above, the induced new band energies E_{\pm} will have more complicate form, but the splitting interval and bandwidth are still related to the t and t' . In this case the effective interaction obtained by themethod of random-phase-approximation (RPA) which provides an excellent approximation for our tight-binding model has the similar form

$$U_{\text{eff}} = \frac{1}{N} \sum_{ab, kk'} \Gamma'^{l_1 l_2}(k, k', \omega) c_{l_1}^\dagger(k) c_{l_1}^\dagger(-k) c_{l_2}(-k') c_{l_2}(k'), \tag{4}$$

with the effective interaction vertex Γ'^{ab} between two Cooper pairs near the FS

$$\Gamma'^{ab}(k, k', \omega) = \text{Re} \sum_{ab, kk'} \Gamma_{a_3 a_4}^{a_1 a_2}(k, k', 0) \Lambda_{a_1}^{l_1*}(k) \Lambda_{a_2}^{l_1*}(-k) \Lambda_{b_1}^{l_2}(-k') \Lambda_{b_2}^{l_2}(k'). \tag{5}$$

Here a_i , $i = 1, 2, 3, 4$ is the cell index and l_i , $i = 1, 2, 3, 4$ is the orbit index. And here we note that the orbital space and the band space are closely connected in the following computations using the RPA method for which the different bands with different eigenvalues.

Considering the bulking distance in the freestanding silicene, the nearest-neighbor hopping vectors may become

$$\begin{aligned}
r_1 = & \left(\frac{\sqrt{3}k_x}{3}, 0, \frac{\sqrt{3}k_z}{3} \tan\theta \right), \\
r_2 = & \left(\frac{-\sqrt{3}k_x}{6}, \frac{k_y}{2}, \frac{\sqrt{3}k_z}{3} \tan\theta \right), \\
r_2 = & \left(\frac{-\sqrt{3}k_x}{6}, -\frac{k_y}{2}, \frac{\sqrt{3}k_z}{3} \tan\theta \right),
\end{aligned} \tag{6}$$

where $\theta \approx 12^\circ 55'$ is the angle between the Si-Si band with the $x - y$ plane, and thus it has $\frac{\sqrt{3}k_z}{3} \tan\theta \approx -\frac{k_z}{2\sqrt{14}}$. while the next-nearest-neighbor hopping vectors \mathbf{r}' are not affected. The

resulting nearest-neighbor dispersion are[7]

$$\epsilon_1 = \begin{pmatrix} \{1, 1, 1\} \\ \{1, \frac{1}{4}, \frac{1}{4}\} \\ \{1, -\frac{1}{2}, -\frac{1}{2}\} \\ \{0, \frac{\sqrt{3}}{2}, -\frac{\sqrt{3}}{2}\} \\ \{0, \frac{3}{4}, \frac{3}{4}\} \\ \{0, -\frac{\sqrt{3}}{4}, \frac{\sqrt{3}}{4}\} \\ \{0, 0, 0\} \end{pmatrix} e^{i\mathbf{k}\cdot\mathbf{r}} = \begin{pmatrix} \{1, 1, 1\} \\ \{1, \frac{1}{4}, \frac{1}{4}\} \\ \{1, -\frac{1}{2}, -\frac{1}{2}\} \\ \{0, \frac{\sqrt{3}}{2}, -\frac{\sqrt{3}}{2}\} \\ \{0, \frac{3}{4}, \frac{3}{4}\} \\ \{0, -\frac{\sqrt{3}}{4}, \frac{\sqrt{3}}{4}\} \\ \{0, 0, 0\} \end{pmatrix} \begin{pmatrix} e^{ikr_1} \\ e^{ikr_2} \\ e^{ikr_3} \end{pmatrix} \quad (7)$$

which make up the sp^3s^* model of silicene consider the σ -band thus the valence (Kohn-Luttinger) band are more lower than the sp^3 one and the σ band and π band can't be crossing with each other in this case, e.g., for the planar silicene the σ band and π band also can't be crossing with each other due to the orbital symmetry unless there exist the intrinsic SOC. The next-nearest-neighbor dispersion are[7]

$$\epsilon_2 = \begin{pmatrix} \{1, 1, 1, 1, 1, 1\} \\ \{1, 1, \frac{3}{4}, \frac{3}{4}, \frac{3}{4}, \frac{3}{4}\} \\ \{1, 1, \frac{1}{4}, \frac{1}{4}, \frac{1}{4}, \frac{1}{4}\} \\ \{1, -1, -\frac{1}{2}, \frac{1}{2}, \frac{1}{2}, -\frac{1}{2}\} \\ \{0, 0, \frac{3}{4}, \frac{3}{4}, \frac{3}{4}, \frac{3}{4}\} \\ \{0, 0, -\frac{\sqrt{3}}{4}, -\frac{\sqrt{3}}{4}, \frac{\sqrt{3}}{4}, \frac{\sqrt{3}}{4}\} \\ \{0, 0, \frac{\sqrt{3}}{2}, -\frac{\sqrt{3}}{2}, \frac{\sqrt{3}}{2}, -\frac{\sqrt{3}}{2}\} \\ \{0, 0, 0, 0, 0, 0\} \end{pmatrix} e^{i\mathbf{k}\cdot\mathbf{r}'} = \begin{pmatrix} \{1, 1, 1, 1, 1, 1\} \\ \{1, 1, \frac{3}{4}, \frac{3}{4}, \frac{3}{4}, \frac{3}{4}\} \\ \{1, 1, \frac{1}{4}, \frac{1}{4}, \frac{1}{4}, \frac{1}{4}\} \\ \{1, -1, -\frac{1}{2}, \frac{1}{2}, \frac{1}{2}, -\frac{1}{2}\} \\ \{0, 0, \frac{3}{4}, \frac{3}{4}, \frac{3}{4}, \frac{3}{4}\} \\ \{0, 0, -\frac{\sqrt{3}}{4}, -\frac{\sqrt{3}}{4}, \frac{\sqrt{3}}{4}, \frac{\sqrt{3}}{4}\} \\ \{0, 0, \frac{\sqrt{3}}{2}, -\frac{\sqrt{3}}{2}, \frac{\sqrt{3}}{2}, -\frac{\sqrt{3}}{2}\} \\ \{0, 0, 0, 0, 0, 0\} \end{pmatrix} \begin{pmatrix} e^{ikr'_1} \\ e^{ikr'_2} \\ e^{ikr'_3} \\ e^{ikr'_4} \\ e^{ikr'_5} \\ e^{ikr'_6} \end{pmatrix} \quad (8)$$

as a sp^3 model which contains the effect of $\pi - \sigma$ rehybridization[8]. It's obviously that the Eq.(1) consider the π -band (mainly contributed by the p -orbit) which contains both the nearest-neighbor hopping and the next-nearest-neighbor hopping, and it can be represented by[7]

$$H_\pi = \begin{pmatrix} E_p + V_{pp\pi}^{\{2\}} e^{i\mathbf{k}\cdot\mathbf{r}'} & V_{pp\pi}^{\{1\}} e^{i\mathbf{k}\cdot\mathbf{r}} \\ V_{pp\pi}^{\{1\}} (e^{i\mathbf{k}\cdot\mathbf{r}})^* & \epsilon_p + V_{pp\pi}^{\{2\}} e^{i\mathbf{k}\cdot\mathbf{r}'} \end{pmatrix} \quad (9)$$

where $V_{pp\pi}^{\{1\}}$ and $V_{pp\pi}^{\{2\}}$ are the first-order and second-order parameters of π band made by the p bands, and E_p is the p band's energy, and

$$H_\pi = \begin{pmatrix} 0 & 0 \\ 0 & 0 \end{pmatrix} \quad (10)$$

only in the point of ($k_x = 0, k_y = 0$), i.e., the gapless Dirac-point (with the heavy particle/hole subband), which have the zero effective mass $m^* = 0$ for the charge carriers. The total

Hamiltonian is (we omitt the $e^{i\mathbf{k}\cdot\mathbf{r}}$ and $e^{i\mathbf{k}\cdot\mathbf{r}'}$ for simplicity in the following)

$$\begin{aligned}
H_{\sigma/\pi} &= \begin{pmatrix} H_{\pi} & N_{2\times 6} \\ N_{6\times 2}^{\dagger} & H_{\sigma} \end{pmatrix}, \\
H_{\sigma} &= \begin{pmatrix} L & T \\ T^{\dagger} & L \end{pmatrix}, \\
T &= \begin{pmatrix} V_{pp\sigma}^{\{1\}}\{1, \frac{1}{4}, \frac{1}{4}\} + V_{pp\pi}^{\{1\}}\{0, \frac{3}{4}, \frac{3}{4}\} & (V_{pp\sigma}^{\{1\}} - V_{pp\pi}^{\{1\}})\{0, -\frac{\sqrt{3}}{4}, \frac{\sqrt{3}}{4}\} & -V_{sp\sigma}^{\{1\}}\{1, -\frac{1}{2}, -\frac{1}{2}\} \\ (V_{pp\sigma}^{\{1\}} - V_{pp\pi}^{\{1\}})\{0, -\frac{\sqrt{3}}{4}, \frac{\sqrt{3}}{4}\} & V_{pp\sigma}^{\{1\}}\{0, \frac{3}{4}, \frac{3}{4}\} + V_{pp\pi}^{\{1\}}\{0, \frac{3}{4}, \frac{3}{4}\} & -V_{sp\sigma}^{\{1\}}\{0, \frac{\sqrt{3}}{2}, -\frac{\sqrt{3}}{2}\} \\ V_{sp\sigma}^{\{1\}}\{1, -\frac{1}{2}, -\frac{1}{2}\} & V_{sp\sigma}^{\{1\}}\{0, \frac{\sqrt{3}}{2}, -\frac{\sqrt{3}}{2}\} & V_{pp\pi}^{\{1\}}\{1, 1, 1\} \end{pmatrix}, \\
L &= \begin{pmatrix} L_1 & L_3 & & 0 \\ L_3^{\dagger} & L_2 & & 0 \\ 0 & 0 & E_p + V_{pp\pi}^{\{2\}}\{1, 1, 1, 1, 1, 1\} + \Delta_{sp} & \end{pmatrix}, \\
L_1 &= E_p + V_{pp\sigma}^{\{2\}}\{0, 0, \frac{3}{4}, \frac{3}{4}, \frac{3}{4}, \frac{3}{4}\} + V_{pp\pi}^{\{2\}}\{1, 1, \frac{1}{4}, \frac{1}{4}, \frac{1}{4}, \frac{1}{4}\}, \\
L_2 &= E_p + V_{pp\sigma}^{\{2\}}\{1, 1, \frac{1}{4}, \frac{1}{4}, \frac{1}{4}, \frac{1}{4}\} + V_{pp\pi}^{\{2\}}\{0, 0, \frac{3}{4}, \frac{3}{4}, \frac{3}{4}, \frac{3}{4}\}, \\
L_3 &= (V_{pp\sigma}^{\{2\}} - V_{pp\pi}^{\{2\}})\{0, 0, -\frac{\sqrt{3}}{4}, -\frac{\sqrt{3}}{4}, \frac{\sqrt{3}}{4}, \frac{\sqrt{3}}{4}\}
\end{aligned} \tag{11}$$

where Δ_{sp} is the energy difference between the $3s$ and $3p$ orbitals, which corresponds to the Kana-Mele term as $\frac{\hbar}{m_0}\langle s|p\rangle$. The next-nearest-neighbor $V_{ss\sigma}^{(2)} = 0$ and $V_{sp\sigma}^{(2)} = 0$ [9], for the specific parameters, see the Refs.[10, 11, 7, 9] and the references therein. We can also know that the $H_{\sigma} \neq 0$ even in the Dirac-point unlike the H_{π} , and don't rely on the effective mass of charge carriers but the rest mass m_0 . In the following, we use continuum approximation around the Dirac-point as $t \sum_{\mathbf{r}} e^{i\mathbf{k}\cdot\mathbf{r}} + t' \sum_{\mathbf{r}'} e^{i\mathbf{k}\cdot\mathbf{r}'} = \hbar v_F \mathbf{k}$ in the following, where $v_F = \hbar \mathbf{k} / (2m)$ for the free electrons.

In the basis of the perturbative $\mathbf{k} \cdot \mathbf{p}$ theory which is widely used for the semiconductor system, with the twofold degenerate dispersion in the Γ -point which is contributed by the p orbitals, and with the bare wave function[12]

$$H = \frac{\hbar}{m_0} \mathbf{k} \cdot \mathbf{p} = \frac{\hbar}{m_0} \mathbf{k} \cdot \langle p_+ | -i\hbar \partial_{\mathbf{r}} | p_- \rangle, \tag{12}$$

with the center momentum formed by two electron states p_+ and p_- with distinct angular momenta, and suffer a perturbation \mathbf{k} . In the case of TRI, the momentum operator has $\mathbf{p} = \mathbf{p}^*$. For two sublattices in a unit cell, the momentum matrix element $\mathbf{p}_{ij} = \langle \psi_A(\mathbf{k}) | \mathbf{p} | \psi_B(\mathbf{k}) \rangle$ which is not zero since the inversion symmetry is broken, and is related to the Wannier function as $\psi_A(\mathbf{k}) = \sum_A w(\mathbf{r} - \mathbf{r}_A) e^{i\mathbf{k}\cdot\mathbf{r}_A}$, $\psi_B(\mathbf{k}) = \sum_A w(\mathbf{r} - \mathbf{r}_B) e^{i\mathbf{k}\cdot\mathbf{r}_B}$.

We represent the total Hamiltonian which under a perturbation (which may be origin from, e.g., an inhomogeneous electric field or electromagnetic wave) as

$$H = H_0(\mathbf{p}) + \delta H(\partial_{\mathbf{r}}) \tag{13}$$

the perturbation tilted the spin order by an angle $\theta = \mathbf{k} \cdot \mathbf{r}$ basis on an initial phase factor ϕ which is defined above. For the Zeeman field-induced perturbation, we can perform the canonical

transformation to the total Hamiltonian as

$$H \rightarrow e^{H_M} H e^{-H_M},$$

$$H_d = \begin{pmatrix} 0 & -M_z \\ M_z^\dagger & 0 \end{pmatrix}, \quad (14)$$

and the SOC term $N_{2 \times 6}$ has the below relation with the Zeeman effect[13]

$$N_{2 \times 6} = M_z H_\sigma - H_\pi M_z, \quad (15)$$

Then the above matrix element T under the perturbation-induced rotation is $T(\mathbf{k}, \partial_{\mathbf{r}}) = \sum_{\mathbf{k}} \mathcal{R}_z^\dagger T(\mathbf{k}) \mathcal{R}_z e^{i\mathbf{k} \cdot \mathbf{r}}$ with the rotation arounds the z -axis as[14, 13]

$$R_z = e^{i\theta} = \begin{pmatrix} \cos\phi & -\sin\phi & 0 \\ \sin\phi & \cos\phi & 0 \\ 0 & 0 & 1 \end{pmatrix}, \quad \theta^{\text{odd}} = \begin{pmatrix} 0 & i & 0 \\ -i & 0 & 0 \\ 0 & 0 & 0 \end{pmatrix}, \theta^{\text{even}} = \begin{pmatrix} 1 & 0 & 0 \\ 0 & 1 & 0 \\ 0 & 0 & 0 \end{pmatrix},$$

$$e^{i\mathbf{k} \cdot \mathbf{r}} R_z = \begin{pmatrix} -\cos\phi \sin(\mathbf{k} \cdot \mathbf{r}) & -\sin\phi & \cos\phi \cos(\mathbf{k} \cdot \mathbf{r}) \\ -\sin\phi \sin(\mathbf{k} \cdot \mathbf{r}) & \cos\phi & \sin\phi \cos(\mathbf{k} \cdot \mathbf{r}) \\ -\cos(\mathbf{k} \cdot \mathbf{r}) & 0 & -\sin(\mathbf{k} \cdot \mathbf{r}) \end{pmatrix}. \quad (16)$$

3 Tight-binding model

Firstly the four-band tight-binding (TB) model for the monolayer silicene in low-energy and under both the perpendicular electron field and exchange field, is given in a non-Hermitian form[15, 11, 16, 18, 17, 2, 19]

$$H_{\text{monolayer}} = t \sum_{\langle i,j \rangle; \sigma} c_{i\sigma}^\dagger c_{j\sigma} + i \frac{\lambda_{\text{SOC}}}{3\sqrt{3}} \sum_{\langle\langle i,j \rangle\rangle; \sigma\sigma'} v_{ij} c_{i\sigma}^\dagger \sigma_{\sigma\sigma'}^z c_{j\sigma'} - i \frac{2R}{3} \sum_{\langle\langle i,j \rangle\rangle; \sigma\sigma'} c_{i\sigma}^\dagger (\mu \Delta(\mathbf{k}_{ij}) \times \mathbf{e}_z)_{\sigma\sigma'} c_{i\sigma'}$$

$$+ i R_2 (E_\perp) \sum_{\langle i,j \rangle; \sigma\sigma'} c_{i\sigma}^\dagger (\Delta(\mathbf{k}_{ij}) \times \mathbf{e}_z)_{\sigma\sigma'} c_{i\sigma'} - \frac{\bar{\Delta}}{2} \sum_{i\sigma} c_{i\sigma}^\dagger \mu E_\perp c_{i\sigma}$$

$$+ M_s \sum_{i\sigma} c_{i\sigma}^\dagger \sigma_z c_{i\sigma} + M_c \sum_{i\sigma} c_{i\sigma}^\dagger c_{i\sigma} + U \sum_i \mu n_{i\uparrow} n_{i\downarrow}, \quad (17)$$

where $t = 1.6$ eV is the nearest-neighbor hopping which contains the contributions from both the π band and σ band. The gap function is $\Delta(\mathbf{k}) = \mathbf{d}(\mathbf{k}) \cdot \boldsymbol{\sigma}$ which in a coordinate independent but spin-dependent representation. The \mathbf{k} -dependent unit vector $\mathbf{d}(\mathbf{k})$ here has $\mathbf{d}(\mathbf{k}) = [t'_{\text{SOC}} \sin k_x, t'_{\text{SOC}} \sin k_y, M_z - 2B(2 - \cos k_x + \cos k_y)]$ for the BHZ model, where B is the BHZ model -dependent parameter and M_z the Zeeman field term which dominate the surface magnetization but can be ignore when a strong electric field or magnetic field is applied. $\langle i, j \rangle$ and $\langle\langle i, j \rangle\rangle$ denote the nearest-neighbor (NN) pairs and the next-nearest-neighbor (NNN) pairs, respectively. $\mu = \pm 1$ denote the A (B) sublattices. Here $\mathbf{d}(\mathbf{k}_{ij}) = \frac{\mathbf{d}_{ij}}{|\mathbf{d}_{ij}|}$ is the NNN hopping vector. $\lambda_{\text{SOC}} = 3.9$ meV is the intrinsic spin-orbit coupling (SOC) strength which is much larger than the monolayer graphene's (0.0065 meV[20]). R is the small intrinsic Rashba-coupling due to the low-buckled structure, which is related to the helical bands (helical edge states) and the

SDW in silicene, and it's disappear in the Dirac-point ($k_x = k_y = 0$). $R_2(E_\perp)$ is the extrinsic Rashba-coupling induced by the electric field. The existence of R breaks $U(1)$ spin conservation (thus the s^z is no more conserved) and the mirror symmetry of silicene lattice. $M = M_s + M_c$ is the exchange field which breaks the spatial-inverse-symmetry and the M_s is related to the out-of-plane FM exchange field with parallel alignment of exchange magnetization and M_c is related to the CDW, which endows sublattice pseudospin the z -component[21]. While for the out-of-plane AFM exchange field M_s^{AFM} which is not contained here with antiparallel alignment of exchange magnetization. Here the M is applied perpendicular to the silicene, and it can be rised by proximity coupling to the ferromagnet[2]. Thus the induced exchange magnetization along the z -axis between two sublattices-plane is related to the SOC, Rashba-coupling, and even the Zeeman-field since it will affects the magnetic-order in z -direction. In fact, if without the exchange field and only exist the SOC, the spin-up and spin-down states won't be degenerates but will mixed around the crossing points between the lowest conduction band and the highest valence band just like the spin-valley-polarized semimetal (SVPSM). Note that here we follow the definition of semimetal that the conduction band and valence band have a small overlap, no matter the two bands are with linear dispersion in the crossing point or parabolic dispersion (quadratic) in the crossing point like the Fermi point of the AB-stacked bilayer silicene or graphene. $v_{ij} = (\mathbf{d}_i \times \mathbf{d}_j) / |\mathbf{d}_i \times \mathbf{d}_j| = 1(-1)$ when the next-nearest-neighboring hopping of electron is toward left (right), with $\mathbf{d}_i \times \mathbf{d}_j = \sqrt{3}/2(-\sqrt{3}/2)$. The term contains the exchange field M is the staggered potential term induced by the buckled structure which breaks the particle-hole symmetry. Here the coordinate-independent representation of the Rashba-coupling terms is due to the broken of inversion symmetry as well as the mirror symmetry. The last term is the Hubbard term with on-site interaction U which doesn't affects the bulk gap here but affects the edge gap. Thus the U is setted as zero within the bulk but nonzero in the edge, which is also consistent with the STM-result of silicene that the edge states have higher electron-density than the bulk. And here we take account the on-site Hubbard interaction only and ignore the long-range ones which are screened by the finite DOS with high energy, like the NN or NNN Coulomb repulsion, interlayer Coulomb repulsion, and even the one with a range much larger than a (like the Bohr radius in semiconductor). For the bilayer silicene, we consider two kinds of the AA-stacked silicene: one with the nearest layer distance as $d = 5.2 \text{ \AA}$ and intra-layer bond length 2.28 \AA with the bulked distance $\bar{\Delta} = 0.46 \text{ \AA}$ the same as the monolayer one and the another one with the nearest layer distance as $d = 2.46 \text{ \AA}$ and intra-layer bond length 2.32 \AA with the lattice constant $a = 3.88$ and the bulked distance $\bar{\Delta} = 0.64 \text{ \AA}$ as plotted in the Fig.1. Thus for the bilayer silicene, the eight-band tight-binding (TB) model in low-energy

Dirac theory is

$$\begin{aligned}
H_{bilayer} = & t \sum_{\langle i,j \rangle, \sigma, l} c_{i\sigma l}^\dagger c_{j\sigma l} + i \frac{\lambda_{SOC}}{3\sqrt{3}} \sum_{\langle\langle i,j \rangle\rangle; \sigma\sigma'} v_{ij} c_{i\sigma l}^\dagger \sigma_{\sigma\sigma'}^z c_{j\sigma' l} - i \frac{2R}{3} \sum_{\langle\langle i,j \rangle\rangle, \sigma\sigma', l} c_{i\sigma l}^\dagger (\mu \Delta(\mathbf{k}_{ij}) \times \mathbf{e}_z)_{\sigma\sigma'} c_{i\sigma' l} \\
& + i R_2(E_\perp) \sum_{\langle i,j \rangle, \sigma\sigma', l} c_{i\sigma}^\dagger (\Delta(\mathbf{k}_{ij}) \times \mathbf{e}_z)_{\sigma\sigma'} c_{i\sigma' l} - \frac{\bar{\Delta}}{2} \sum_{i\sigma l} c_{i\sigma l}^\dagger \mu E_\perp c_{i\sigma l} \\
& + M_s \sum_{i\sigma l} c_{i\sigma l}^\dagger \sigma_z c_{i\sigma l} + M_c \sum_{i\sigma l} c_{i\sigma l}^\dagger c_{i\sigma l} + U \sum_{i,l} \mu n_{i,l\uparrow} n_{i,l\downarrow} + t_1 \sum_{i,\sigma,l} c_i^\dagger c_j \\
& + i \lambda_{SOC}^{\text{int}} \sum_{i \in A_1, j \in A_2, \sigma} c_{i\sigma}^\dagger (\mu \Delta(\mathbf{k}_{ij}) \times \mathbf{e}_z)_{\sigma\sigma'} c_{i\sigma'} \\
& + i \lambda_{SOC}^{\text{int}} \sum_{i \in B_1, j \in B_2, \sigma} c_{i\sigma}^\dagger (\mu \Delta(\mathbf{k}_{ij}) \times \mathbf{e}_z)_{\sigma\sigma'} c_{i\sigma'} \\
& + \begin{cases} t_3 \sum_{i \in A_1, j \in A_2, \sigma} c_{i\sigma}^\dagger \mu c_{j\sigma} + t_2 \sum_{i \in B_1, j \in B_2, \sigma} c_{i\sigma}^\dagger \mu c_{j\sigma}, & \text{for 2nd AA - stacked bilayer silicene,} \\ t_1 \sum_{i \in A_1, j \in A_2, \sigma} c_{i\sigma}^\dagger \mu c_{j\sigma} + t_1 \sum_{i \in B_1, j \in B_2, \sigma} c_{i\sigma}^\dagger \mu c_{j\sigma}, & \text{for 1st AA - stacked bilayer silicene,} \end{cases}
\end{aligned} \tag{18}$$

where $l = \pm 1$ is the layer index, and $\lambda_{SOC}^{\text{int}} = 0.5$ meV is the interlayer SOC[22].

Note that for low-energy case the energy spectrum is $\varepsilon_\eta(\mathbf{k}) = \sqrt{\hbar^2 v_F^2 \mathbf{k}^2 + m_D^2}$ where m_D is the Dirac mass generated by the bulk-gap-open through the spontaneous symmetry breaking by applying the optical field, electric field, magnetic field as explored in Ref.[15], even without the Zeeman splitting. $\eta = \pm 1$ is the valley index for the K and K' valley. While for the higher energy relativistic case, the Dirac-mass term in above energy spectrum expression show be replaced by mv_F^2 with the relativistic mass m .

In the above TB model, both the NNN (linear-Rashba) and NN (electric-field-induced) Rashba-coupling is considered, Since there without the contributions from Dresselhaus term, the spin SU(2) symmetry is broken together with the effect of NNN SOC term λ_{SOC} , but the valley SU(2) symmetry may remains.

In the presence of both the E_\perp and the first-order and second-order Rashba-coupling, the system can be described by $H = \Psi^\dagger H_{\text{eff}}^\pm \Psi / 2$, the BCS-like effective Hamiltonian of the neighbor valleys by the low-energy Dirac theory in the basis of $\{\tau \otimes \sigma\}$ which reflected in the two-component spinor-valued field operators as $\Psi = [(\psi_\uparrow^A, \psi_\downarrow^A, \psi_\uparrow^B, \psi_\downarrow^B), ((\psi_\uparrow^{A\dagger}, \psi_\downarrow^{A\dagger}, \psi_\uparrow^{B\dagger}, \psi_\downarrow^{B\dagger}))]^T$, are

$$\begin{aligned}
H_{\text{eff}}^+ &= \begin{pmatrix} \mathcal{H}(\mathbf{k}, \sigma_z) & \Delta(\mathbf{k}, \sigma_y) \\ \Delta^\dagger(\mathbf{k}, \sigma_y) & \mathcal{H}(\mathbf{k}, -\sigma_z) \end{pmatrix}, \\
\mathcal{H}(\mathbf{k}, \sigma_z) &= \lambda_{SOC} \sigma_z \tau_z + aR(k_y \sigma_x - k_x \sigma_y \tau_z) + M \tau_z \sigma_z - \frac{\bar{\Delta}}{2} E_\perp \tau_z + \frac{R_2(E_\perp)}{2} (\sigma_y \tau_x - \sigma_x \tau_y), \\
\Delta(\mathbf{k}, \sigma_y) &= \begin{pmatrix} i\Delta_A & 0 \\ 0 & i\Delta_B \end{pmatrix}, \\
\Delta_A &= k_y \sigma_y - ik_x \sigma_x, \\
\Delta_B &= -k_y \sigma_y - ik_x \sigma_x,
\end{aligned} \tag{19}$$

and

$$H_{\text{eff}}^- = \begin{pmatrix} \mathcal{H}(\mathbf{k}, -\sigma_z) & -\Delta(\mathbf{k}, -\sigma_y) \\ -\Delta^\dagger(\mathbf{k}, -\sigma_y) & \mathcal{H}(\mathbf{k}, \sigma_z) \end{pmatrix}, \tag{20}$$

Δ_A and Δ_B are the pairing gaps of two sublattices. In the case for valley-polarized metal phase (i.e., the SDC state) which is achievable under the effect of both the vertical electric field[2] or magnetic field[23] and the exchange magnetization especially under the such a strong SOC

which will further intensify the particle-hole asymmetry between the two valleys. with the broken sublattice-pseudospin symmetry but remain the chiral symmetry between two valleys, and the valley-hybridization-term $\Delta(\mathbf{k}, \sigma_y)$ in H_{eff}^+ can be replaced by

$$\mathcal{V}(\mathbf{k}) = \begin{pmatrix} \sqrt{\mathcal{V}_1} & -\sqrt{\mathcal{V}_2}(k_x + ik_y) \\ -\sqrt{\mathcal{V}_2}(k_x - ik_y) & \sqrt{\mathcal{V}_1} \end{pmatrix}, \quad (21)$$

which is proportional to the exchange effect between two sublattices (or the potential difference between two sublattices) with \mathcal{V}_1 the hybridization gap which is also proportional to the potential difference and \mathcal{V}_2 the parabolic band dispersion which with a opened gap. The low-energy effective Hamiltonian can be written as[18, 17]

$$H = \eta\hbar v_F(\tau_x k_x + \tau_y k_y) + \eta\lambda_{\text{SOC}}\tau_z\sigma_z + aR\eta\tau_z(k_y\sigma_x - k_x\sigma_y) - \frac{\Delta}{2}E_{\perp}\tau_z + \frac{R_2(E_{\perp})}{2}(\eta\sigma_y\tau_x - \sigma_x\tau_y) + M\tau_z\sigma_z, \quad (22)$$

and with the eigenvalue

$$\varepsilon_{\eta}(\mathbf{k}) = Ms_z \pm \sqrt{\hbar^2 v_F^2 \mathbf{k}^2 + \left(\frac{\Delta}{2}E_z + \eta\hbar m_w - \eta s_z \lambda_{\text{SOC}}\right)^2}. \quad (23)$$

For the bilayer silicene, the BCS-like effective Hamiltonian can be expressed as

$$H_{\text{eff}}^{\text{bilayer}}(\mathbf{k}) = \begin{pmatrix} H_{\text{eff}}^+ & t_{\text{inter}} \\ t_{\text{inter}} & H_{\text{eff}}^- \end{pmatrix}. \quad (24)$$

and the corresponding eigenvalue (band dispersion) is[24]

$$\varepsilon'_{\eta}(\mathbf{k}) = \pm \sqrt{m_D^2 + \left(\frac{t_{\text{inter}}}{\sqrt{2}}\right)^2 + \hbar^2 v_F^2 \mathbf{k}^2 + l \sqrt{\left(\frac{t_{\text{inter}}}{\sqrt{2}}\right)^4 + \hbar^2 v_F^2 \mathbf{k}^2 \cdot (t_{\text{inter}}^2 + (2m_D)^2)}}. \quad (25)$$

The bands obtained by this eigenvalue are shifted upward by the positive t_{inter} and downward by the negative t_{inter} , which corresponds to the antibonding and bonding states, respectively. And the energy of antibonding states are increased with the increasing scattering strength, and reaches the maximum in the critical point as we detect below. The interaction terms, like the strong intrinsic SOC are contained in the Dirac mass term of the above expression, and it also valid for the gap-anisotropy case, which increase when the long-range Hubbard interactions are taken into consider, or the long-range hopping case, like the NNN hopping.

The vertex correlation function Γ is associated with the jumping of the self-energy with different spectral weight in momentum space, and it plays a important role in the variant cluster approximation (VCA). For the impurities scattering system, the vertex correlation function is arise with the lifting of Fermi level (E_F), which leads to the segmental structure of energy spectrum. and thus increase the cancellation effect[25] to the Hall conductivity. Otherwise it can be ignored if Fermi energy E_F is close to zero with a very low FS and thus it's completely spin-dependent. While for the interband longitudinal conductivity, it will vanishes when there exists linear R and linear Dresselhaus coupling with equal strength[26]. Although the vertex function is piecewise for a finite Fermi energy and in the direction which normal to the boundary between different pieces with different self-energies (or momentum), it can be ignored for the case of $m_D = 0$, $t_{\text{inter}} = 0$ through the vertex renormalization[27] and the conductivity can be evaluated by the bubble approximation.

We carry out the first-principle (FP) density functional theory (DFT) calculations using the QUANTUM ESPRESSO package[28] with the generalized gradient approximation (GGA), and the Perdew-Burke-Ernzerhof (PBE)[29] exchange correlation is used. The plane wave

energy cutoff is setted as 250 eV in our calculation, and the structures are relaxed until the Hellmann-Feynman force on the atoms are below 0.01 eV/Å . As shown in the Fig.3(a), the band structure of monolayer silicene shows linear and isotropic relations $\varepsilon = \pm\sqrt{3}t|\mathbf{k} - \mathbf{K}|/2$ near the Dirac-point (and also the for DOS) which suggest a energy-independent group velocity v_g even it's slightly gapped up, while the bilayer silicene dose not. The pseudogap in the such point suggests the semi-metal phase of silicene which can be charged to other phase through the tunable phase transitions in the nanodisk, nanotube, or nanoribbon silicene[15]. While the linear dispersion in M -point is exist only in the small- a limit. Note that here we consider the case that the Fermi level lies within in the band gap (the lowest conduction band and the highest valence band) and at the point with $\mu = 0$. The DOS of monolayer silicene and AA-stacked bilayer silicene are presented in the right-side of the Fig.3. We found that the PDOS of 1st AA-stacked bilayer silicene almost has the same shape with the monolayers', but just twice in the amount. For the 2nd AA-stacked bilayer silicene (Fig.3(c)), which remain the semimetal but the two linear-crossing Dirac-point drift away from the K-point, and one lies above the Fermi level while the other one lies below the Fermi level which is different from the bilayer graphene. The total DOS of 2nd AA-stacked bilayer silicene is not zero at Fermi level similar to the AB-stacked graphene, and exhibit great difference with the monolayer one and the 1st AA-stacked bilayer one. Thus we only explore the DOS of the monolayer silicene and 2nd AA-stacked bilayer silicene in the following. The presented band structure of AA-stacked bilayer silicene shows more strong hybridization between the lowest conduction band and highest valenc band in low-energy than the AB-stacked one. For the antiferromagnetic (AFM) silicene, the AFM spin order with the NN sublattice pairing (like the Cooper pairs) symmetry $d_1 + id_2$ with chiral superconductivity (SC) is supported by the strong electron-electron repulsive interaction especially at the singular value of DOS like the graphene [15] and with the phase winding number 2π around the whole hexagonal lattice (or Brillouin zone) (or 4π [30] around the Fermi surface (FS) which is hexagonal at full band filling v_f when undoped). The SC pairing strength (or SC gap) $\Delta_{SC} = \Delta_0 e^{i\theta}$ where θ is the SC phase as shown in the Fig.1(c). But for highly spin-polarized case, like the edge states in the single-Dirac-cone (SDC) phase which with one valley has gapless bulk gap and has also been found in several kinds of three-dimension TI[31], the lifted ferromagnetic (FM) may give rises the NNN FM pairing correlation with the p -wave or f -wave spin-triplet pairing.

Fig.3(d) shows the single particle DOS for the massless Dirac-fermion in the absence of the impurity and lattice defect. The linear relation appear in the low-energy region $E \ll t$, which is guaranteed by the high order correction of the dispersion in the renormalization group theory[30]. It exhibit great difference with that for the spinless noninteracting case (including the interlayer interaction). The DOS-map is calculated by the RG method with the linear dispersion constricted in the bandwidth in the range π -band -6.4 eV~6.4 eV, and the UV cutoff within this RG procedure is setted much smaller that the bandwidth which is $\Lambda \simeq t = 1.6$ eV.

In Fig.4, we show the map plot of the tight-binding energy dispersion and the corresponding DOS for the silicene with particle-hole symmetry where we ignore the broken of inversion symmetry by the bulked structure and the Rashba-coupling (NNN). In Fig.4(a), we consider the dispersion in hexagonal BZ with the contribution only from π -electron, $t = V_{pp\pi}^{(1)}$ (which measured as -0.72 in Ref.[7] and -1.12[11]): $\varepsilon_{\text{hex}} = \pm t\sqrt{1 + 4\cos^2(k_x a/2) + 4\cos(k_x a/2)\cos(\sqrt{3}k_y a/2)}$. Since the zero-energy point in DOS corresponds to the spin-degenerate point and the Fermi level is in the place with $\mu = 0$, when the upper band (conduction band) is empty, the lower one is fully filled, and then give rise to the maximum spin-polarization with the minimum interaction strength to minimized the system energy due to the Hund's rule. That's also consist with the zero-energy state in the gapless Dirac-point. In this case the total spin is becomes maximum as $\hbar N/2$ ideally in the ferromagnetic ground state where N is the number of electrons which equal

to four times of the cell number in the four band model (doubly degenerate). Such fully spin-polarized pattern also appear in the case of SDC and the spin-valley TI as we disussed in the Ref.[15], and it also excludes the double occupation at half-filling $d_{hf} = \sum_i n_{i\uparrow}n_{i\downarrow}/N$. and thus makes the method of dynamical mean-field theory (DMFT) which with the HartreeFock term and it is efficient to dealing with the nonequilibrium problem with different bandgaps[15, 32] lose efficacy in the single-site problem[33]. What's more, the critical value derived from the DMFT: $U=2.23t$ [34], is far away from our result obtained in the follwing text, which is $9 \text{ eV} \approx 5.6t$ for the pure monolayer silicene and $12 \text{ eV} \approx 7.5t$ for the monolayer silicene with impurity. That's due to the DMFT ignore the quantum fluctuation and the up-spin are independent with the down-spin, and thus there exist great deviation from the ture results in our model, which with drastic spin and charge fluctuations. That can also be seem from the large otherness from the semielliptic DOS derived from the DMFT (see Ref.[15]) to our results.

The in-plane spin texture (σ_x and σ_y) can be obtained by the spin expectation values as[26] $s_{x\pm} = \pm \frac{\hbar}{2} \frac{\mathcal{R}}{\sqrt{\mathcal{R}^2 + \mathcal{R}_2^2}}$, $s_{y\pm} = \pm \frac{\hbar}{2} \frac{-\mathcal{R}_2}{\sqrt{\mathcal{R}^2 + \mathcal{R}_2^2}}$, with $\mathcal{R} = (a\eta\tau_z Rk_y - \frac{R_2(E_{\perp})}{2}\tau_y)$, $\mathcal{R}_2 = (-a\eta\tau_z Rk_x + \frac{R_2(E_{\perp})}{2}\tau_x)$, and the \pm here corresponds to the sign of Rashba energy $E = \frac{m(R^2 + (R_2(E_{\perp})^2))}{2\hbar^2}$. While the out-of-plane spin texture is related to the Dirac mass and the Zeeman splitting. The group velocity through the above Dirac Hamiltonian as $v_{gx} = \frac{\partial \mathcal{H}}{\hbar \partial k_x} = v_F \eta \tau_x - \frac{1}{\hbar} a \eta \tau_z R \sigma_y$, $v_{gy} = \frac{\partial \mathcal{H}}{\hbar \partial k_y} = v_F \tau_y + \frac{1}{\hbar} a \eta \tau_z R \sigma_x$. The effect of Rashba-coupling to the DOS is exploed in the following section.

4 DOS

In the energy-dependent density of state (DOS), the van Hove singularities (VHS) emerge at the band filling $\delta = \pm t$ away from the Dirac-point and with the FS nesting which with infinity (impurity) quasiparticle lifetime. Although the large DOS in the VHS effectively enhance the effect of interaction, the strength of interaction is linearly increase with the increasing scattering rate and the logarithmically divergent DOS toward the Dirac-point. The large DOS in VHS also effectively screen the long-range Coulomb repulsion, and diverges the susceptibility. The VHS also exhibit peak signal in the twisted silicene or graphene due to the new saddle point created by the ratotaed Dirac-point which are still in the K-point[35]. The VHS origin by the saddle points of π and π^* bands in BZ which is the in the M -point for unstrained silicene, are keep away from the K-point to persist the semimetal phase, and plays a important role in the phase transition to the metal or the band insulator with sizeble bulk gap. The strong on-site Hubbard interaction (repulsive) also give rise the chiral SC in the bilayer silicene or the graphene[30], while the long-range Hubbard interaction are screened in this point. For the case with the lattice defects like the impurities (dopant) or vacancy, the K-point may exhibits a peak of the δ -function which is obviously smeared by a finite width related to the strength of the impurities or the size of the vacancy, and makes the quasiparticle lifetime τ turn to maximum value (setted as 1) in this case and note that the impurities scattering rate which is defined always always ≥ 0 is $\Gamma = 1/(2\tau) \rightarrow \infty$ here. That's very different from that in the noninteracting limit as well as the case of Hubbard $U=0$. The impurities scattering potential after the Fourier transformation is $V(\mathbf{k}_s) = \frac{2\pi U}{\sqrt{(\Delta\mathbf{k})^2 + k_s^2}}$ with the coulomb potential $U = \frac{qq'}{4\pi\epsilon_0\epsilon_s}$ where $\epsilon_0 = 1$ is the vacuum dielectric constant and $\epsilon_s = 34.33$ is the dielectric constant of silicene. $\Delta\mathbf{k} = |\mathbf{k} - \mathbf{k}'| = 2k \sin\theta$ [36, 37], where θ describes the difference between the momentums before scattering and after scattering, and it tends to zero $\theta \rightarrow 0$ for the SC silicene (deposited on a SC electrode or generate the topological superconductor by the STM probe). The $\Delta\mathbf{k}$ is zero only for the elastic scattering in which case the scattering potential is close to a δ -function similar to the Lorentzian representation and become $\Delta\mathbf{k}$ - and

\mathbf{k}_s -independent. In this case, the scattering potential is decay as $1/|\mathbf{k}_s|$. Due to the exist of the impurities and lattice defects, the quantum spin-Hall effect with the spin-polarized current may more observable due to the SOC with the impurities, even without applying the external exchange field or the electric field, and it's robust against the nonmagnetic impurity.

At the time-reversal symmetry and particle-hole symmetry points of momentum space[15], the nonchiral umklapp backscattering term (not contains the forward scattering exchange J_z) which is[38]

$$J_z a \int dx e^{-i\phi} \psi_{L\uparrow}^\dagger(x) \psi_{L\uparrow}^\dagger(x+a) \times e^{-i\phi} \psi_{R\downarrow}^\dagger(x) \psi_{R\downarrow}^\dagger(x+a) + h.c. \quad (26)$$

in Fermion language is allowed, where $\phi = \varphi x$ with the left move and right move Néel order $\varphi = \pi$ (half of the phase of Wigner-Seitz unit cells) and with the scaling dimension just be one Luttinger parameter K [39] at commensurate filling[38] where the phase transition to a insulator with gap happen. g is the scattering strength factor. And here the renormalized Fermi velocity has $v_F = 1 + \frac{J_z a}{\pi \hbar v_F} (1 - \cos(2k_F a))$. While the chiral term renormalize the Fermi velocity in the homogeneate system without the domain wall, the inhomogeneate case will be discuss below. For umklapp scattering, $\Delta \mathbf{k}$ provides a estimation for the momentum transfer on the semimetal Dirca-sea, and it's proportional to the change of DOS compared to the Fermi momentum k_F before scattering.

In low-temperature, since the elastic scattering is dominate, we can simplify the scattering potential as a δ -function which is momentum-independent with $\mathbf{k} \approx \mathbf{k}'$ thus $\theta \approx 0$. Then without spin-degenerate, the longitudinal in-plane conductivity (diagonal) in linear response theory is[40]

$$\sigma_{xx} = \sigma_{yy} = \frac{\beta e^2}{S} \sum_m f_m (1 - f_m) \frac{\langle m|v_x|m\rangle \langle m|v_y|m\rangle}{\omega + i\delta + 2\Gamma} \quad (27)$$

where $S = 3\sqrt{3}/2$ is the area of unit cell, $\omega = (2n+1)\pi/\beta$ is the fermionic Matsubara frequency where β is the inverse temperature. $v_x = \frac{\partial}{\hbar \partial k_x}$ is the velocity operator. Here $\sigma_{xx} = \sigma_{yy}$ is tenable for the low-temperature in which the elastic scattering is dominate, and with velocity operators in the matrix-form: $v_x = \begin{pmatrix} 0 & v_F \\ v_F & 0 \end{pmatrix}$, $v_y = \eta \begin{pmatrix} 0 & i v_F \\ -i v_F & 0 \end{pmatrix}$. While the transverse off-diagonal in-plane conductivity for the nonelastic scattering is

$$\sigma_{xy} = \frac{i\hbar e^2}{S} \sum_{m \neq n} \frac{f_m - f_n}{(E_n - E_m + \hbar(\omega + i\delta) + i\Gamma)(E_m - E_n)} \langle m|v_x|n\rangle \langle n|v_y|m\rangle. \quad (28)$$

The scattering rate Γ here is defined as

$$\Gamma = \frac{1}{2\tau} = \frac{\pi n}{\hbar} V^2. \quad (29)$$

Here the charged impurity density n is momentum-independent for the single-impurity case. The Γ can be estimated as $0.01t = 0.016$ eV here and note that the effect of SOC is ignored in this scattering process. If the SOC is taken into consider in the collision process of the impurity scattering as done in the explores of spin-Hall effect[41] with the presence of electric currence and the spin currence, the Γ becomes $< \frac{1}{2\tau}$ and thus the DOS may be increased. In the domination of impurity scattering and with a certain impurity concentration, the spin currence can be described by angle θ in Maxwell theory. with the spin-palarized currence perpendicular to the applied electric field which exhibit the quantum quantum anomalous Hall (QAH) effect[15].

5 Results and discussion

The local DOS provides a good estimation for the diagonal longitudinal conductivity which relies on the interband transitions and in contrast with the intraband transverse conductivity, and can be expressed as

$$D(\mathbf{k}, \omega) = \int_{BZ} \frac{d\mathbf{k}}{(2\pi)^2} (f_m - f_n) \text{Im}(G_{\mathbf{k}}(E_m - E_n) - G_{\mathbf{k}}(E_n - E_m)), \quad E_m < E_n, \quad (30)$$

where $f_m = 1/(e^{\beta(E_m - \mu)} + 1)$ is the Fermi-Dirac distribution function with μ the chemical potential in Fermi level, which makes it more like a joint DOS (JDOS) but not a single particle DOS, and the lattice Green's function in helicity basis $G_{\mathbf{k}}(E_m - E_n) = [E_m - E_n - (\hbar\omega + i2\Gamma) - \mu]^{-1}$ which can be obtained by the retarded form analytical continuation as $i\hbar\omega_l \rightarrow \hbar(\omega_l + i\delta)$ [15] where $\delta = 0^+$ is a small positive quantity and it has $\omega + i\delta \rightarrow 0$ in dc-limit. The Fermi-Dirac distribution function can be replaced by the Heaviside step function θ in the zero-temperature limit e.g., $f = 1$ for the electron-like (occupied) band, and $f = 0$ for the hole-like (unoccupied) band and with the Fermi level lies between them. E_m and E_n are the energies of two distinct electron states. To see the effects of the Rashba-coupling on the DOS with the spin expectation values deduced in above, we show the contributions from the Rashba-coupling to the positive-DOS, $D_R(\mathbf{k}, \omega)$, in Fig.6 where only the NN Rashba-coupling is taken into consider and with the applied perpendicular electric field ranges from zero to 8 eV. Fig.6(a) is for the case that Fermi level is lies within the conduction band and valence band (with $\mu = 0$), and (b) is for the case that Fermi level is lies in the conduction band with $\mu = 1$. We see that with the increase of μ , the $D_R(\mathbf{k}, \omega)$ is reduced and the starting point of the transverse axis is shifted. Except that, the sequence of the initial slopes are changed too: the largest slope corresponds the $E_{\perp} = 1$ eV ($R_2 = 0.012$ eV) in the $\mu = 0$ case, while it corresponds the $E_{\perp} = 2$ eV ($R_2 = 0.024$ eV) in the $\mu = 1$ case.

We also found that for monolayer silicene, the DOS in zero-temperature-limit (the silicene is most stable now and similar to the results of non-interacting case) is simply determined by the Dirac-mass, with the certain degenerate number (or degrees of freedom) 4, as shown in the Fig.5(a), which is

$$\rho_{T \rightarrow 0}(\varepsilon, \omega) = \frac{4|\varepsilon|}{2\pi\hbar^2 v_F^2} \frac{1}{2} \sum_{\eta=\pm 1} [\theta(|2\varepsilon| - 2|m_D|\eta)], \quad (31)$$

and the Dirac-mass here is setted as $m_D = |\lambda_{SOC} + M| = 1$ eV. For bilayer silicene in zero-temperature-limit, the DOS is also dependent on the Dirac-mass, but the width of the minimum DOS-plateau is the same as the monolayer silicenes', i.e., $2|m_D|$, but difference from the AB-stacked bilayer one, and the value of this minimum DOS-plateau is depends on the band structure in the Dirac-point. Fig.5(b) shows the diamagnetic susceptibility which is negative in the low-temperature region for the monolayer silicene. In fact, both the diamagnetic and paramagnetic response which with opposite magnetic moment (i.e., diamagnetic moment and paramagnetic moment with the spin carriers along the edge direction carriers the up- and down-spin, respectively) are coexist in the silicene due to the interactions between the magnetic field and the charge carriers with spin-up and spin-down, respectively, and they are both increase with the temperature.

In the presence of nonzero impurity scattering angle with a single impurity, the above expression can be rewritten as

$$D(\mathbf{k}, \omega) = \int_{BZ} \frac{d\mathbf{k}}{(2\pi)^2} (f_m - f_n) \text{Im}[G_{\mathbf{k}}(E_m - E_n)T(\omega)G_{\mathbf{k}}(E_m - E_n + \Delta\mathbf{k}) - G_{\mathbf{k}}(E_n - E_m)T(\omega)G_{\mathbf{k}}(E_n - E_m + \Delta\mathbf{k})], \quad (32)$$

The expression of the DOS is distinct from the conductivity since it takes the imaginary part of the lattice Green's function in the defect configuration. Here the effect of $T(\omega)$ is similar to the vertex function except that the vertex function is a connection between different frequencies but with the same momentum while the $T(\omega)$ here is a connection between different momentums which is related to the scattered wave vector but with the same frequency. And here the direction of $T(\omega)$ is perpendicular to the boundary between the two distinguish momentum tiles, which is weighted by the DOS or the spectral function[42, 33, 43] and is useful to explore the low-energy behaviours of optical conductivity and the Hall conductivity. For the nonmagnetic impurity (or the weak magnetic ordering impurities like W- or Mo-silicene), the $T(\omega)$ has[44]

$$T^{-1}(\omega) = \frac{1}{V_s \sigma_z} - \int \frac{d^2 k}{4\pi^2} G_{\mathbf{k}}(E_m - E_n) \quad (33)$$

where V_s is the single scalar scattering with the z -direction spin-polarization.

Fig.7(a) shows the effect of Hubbard U to the JDOS of monolayer AFM silicene with a half-filled impurity band in the middle. We can see that the sharp of the JDOS-curve have not obviously changes for the Hubbard $U \leq 12$, and the bandwidth is slightly increased. Up to $U \geq 13$, the Fermi level was lifted up to the conduction band in a large extent with increasing DOS and leading to a enlarged chemical potential, similar to the effects of the high doping, and the bandwidth also largely increased to 4 eV in $U = 18$ eV which obviously exhibits the band insulator phase. Thus it's direct that the critical U , which is insensitivity to the strength of impurities, for such a change is around 12 eV (about $7.5t$) which is slightly smaller than that of the graphene which is 13.29[34], but close to the value predicted by the Brinkman-Rice analysis which is 11.5 for the 2D Hubbard model[45]. And it's nearly twice as large as the critical value of the phase transition of metal-to-insulator for the half-filling $1/r$ Hubbard chain, which is equal to the bandwidth whose absolute value is 6.4 eV for silicene[32, 46]. That also implys that the critical value of Hubbard U is associated with the dimension like the DOS distribution[47]. For FM monolayer silicene with nonzerp spin-polarization, the curves of JDOS shows the similar behavior but just with larger band gap between the conduction band and the valence band which we not show here. From Fig.7(b) and (c), we can see that the larger the Hubbard U is, the wider the JDOS-curve expand in the low-energy region. While in the positive-energy-region, the most dominantly curve is the one in critical- U and gradually decrease when away from the critical- U . (see the distribution of antibonding states in Fig.7(c) in the range of $E > 10$ eV). Thus the scattering strength is reaches the maximum at the point of critical U . In these DOS plots, we also found that the p -band is dominate no matter how large the U is, except for the low-energy region. For the pure monolayer silicene and 2nd AA-stacked bilayer silicene (Fig.7(d) and (e), respectively), the critical Hubbard U for the transition from semimetal phase to insulator is 9 eV and 12 eV, respectively.

We next do a dynamical analysis for the in-plane ac conductivity of monolayer silicene. Here we comment that for the 1st AA-stacked bilayer one, the Hall conductivity of the clear sample (without impurity) shows differences with the monolayer one, like the appearance of the $\sigma_{xy} = 0$ plateau, which disappear in the monolayer due to the gapless Dirac-coone when without the electric field or exchange field but with the effective SOC and Rashba-coupling (see Ref.[15]). The $\sigma_{xy} = 0$ plateau is appears in the case that the chemical potential $|\mu| < \min\{t_{\text{inter}}\}$ where t_{inter} is the interlayer hopping[48], since the gapped characteristic as shown in the band structure of Fig.2. The in-plane optical conductivity of monolayer silicene with a finite impurity strength, $\sigma(\Omega) = \sigma_{xx} + \sigma_{yy}$ is shown in the Fig.8, which with the peaks center around 5 eV. The origin of these peaks is associated with VHS in the DOS[49]. Here we note that the momentum change can be evaluated as $\Delta \mathbf{k} = \hbar(\Omega + i\delta)$ in the analytic continuation with the bosonic frequency (photon) Ω . The above critical value of Hubbard U which close to 12 eV is also valid for the in-plane longitudinal conductivity as we shown in the figure. From Fig.8, we find that there

is a large decrease of the value of conductivity in the critical-U both for the real part and the imaginary part. That also exhibit a behavior that transfer to the band insulator phase, where we use a dash-line to divides the two parts (semimetal phase and insulator phase).

This critical-U is also far away from that of the Kane-Mele-Hubbard (KMH) model phase diagram which is $U=4.3t$ measured by the method of Quantum Monte Carlo (QMC) as we did in the Ref.[15]. In the KMH model for the hexagonal lattice at half-filling, the semimetal phase transfer to the AFM Mott insulator at the critical $U=4.3t$ for the case of only consider the NN hopping. A analogous value obtained by QMC which is $4.5t$ is reported in Refs.[47, 50]. But the common points with our present model is that the phase transition of nonmagnetic semimetal phase to the AFM Mott insulator will becomes the paramagnetic phase to the AFM Mott insulator when consider the long-range hopping (like the t'), and the strength of SDW would be reduced compared to the $d_1 + id_2$ SC. While for the phase transition from the AFM order Mott insulator to the semimetal can be realized by increasing the strength of exchange field to a value comparable with λ_{SOC} [2], in this process the AFM superexchange enhance the correlations between the singlet pairing and may results in the valence band resonance (RVB), which can also be realized by the manipulation of the impurities AFM correlation by the impurity doping. The AFM correlation term of the impurities here can be written as $\sum_{\langle i,j \rangle} J_{ij}(S_i S_j - 1/4)$ [51], where the superexchange factor $J_{ij} = 4t^2/U$ in the AFM region is estimated as in the range of 0.85 to 1.49 in our model. The optical conductivity below the critical value also become numb with the change of U unlike the ones above the critical value. After the quenching of the kinetic energy in the microcosmic process due to the momentum transfer, in equilibrium stage, the peak is the mid-infrared peak local at the frequency as twice of the exchange scale[52]. It's also clearly that the peaks of optical conductivity is shift rightwards with the increase of U, which also exhibits the decrease of the strength of electron-phonon interaction, i.e., the electron-phonon interaction red-shift the absorption features of optical conductivity spectra[53]. With the increase of on-site Hubbard U, the kinetic energy also decrease with the increasing quasiparticle mass.

Using the random-phase-approximation (RPA) approach, the above-mentioned long-range Hubbard repulsion (NN Hubbard repulsion) could be screened by the high energy state which with large charge DOS (like the VHS). The screened in-plane long-range Hubbard repulsion can be written as

$$g_s(\mathbf{k}, \omega) = \frac{g}{1 - 4g\Pi(\mathbf{k}, \omega)}, \quad (34)$$

where g is the universe Coulomb repulsion as $g = 2\pi e^2/(\epsilon_0 \mathbf{k})$. The factor 4 here denotes the number of degenerate (or the flavors). Here the wave vector \mathbf{k} denotes the position in the momentum space which not restricted around the Dirac-point, and it can be replaced by v_F to obtain the dimensionless long-range form[27] g_0 . Here we comment that with the increase of this dimensionless Coulomb repulsion g_0 , the linear relation of DOS in low-energy tends to quadratic relation[54]. The denominator of the above expression can be view as the non-static dielectric function $\epsilon^{-1}(\mathbf{k}, \omega)$ obtained by RPA, where the energy loss function L can be well obtained through the relation $L = \text{Im}\epsilon^{-1}(\mathbf{k}, \omega)$ as shown in Ref.[15]. Or in the optical language, the above dielectric function can be rewritten as $\epsilon^{-1}(\mathbf{k}, \omega) = 1 - \frac{8\pi^2 c_s}{\mathbf{k}} \Pi(\mathbf{k}, \omega)$, where c_s is the Sommerfeld vacuum fine structure constant $c_s = \frac{e^2}{2\epsilon_0 hc} = 1/137.036$ [55]. which is related to the zero- ω optical absorption in the limit of vanishing SOC by $A_{op}(0) = \pi c_s$ [56], and is applicable for all of the group IV atoms. The complex polarization function (or the susceptibility) $\Pi(\mathbf{k}, \omega)$ can be deduced from the retarded current-current correlation function in bubble diagram as[57, 24]

$$\Pi(\mathbf{k}, \Omega) = -\frac{4e^2}{\beta} \int \frac{d^2k}{4\pi^2} \text{Tr}[v_\alpha G_{\mathbf{k}}(i\omega + \Omega + i\delta)v_\beta G_{\mathbf{k}}(i\omega)], \quad (35)$$

where $G_{\mathbf{k}}(i\omega) = \int_{-\infty}^{\infty} \frac{d\omega}{2\pi} \frac{A(\omega, \mathbf{k})}{i\omega + \mu - \omega}$ with $A(\omega, \mathbf{k})$ the spectral weight. v_α and v_β denote the two

velocity operators with the leads $\alpha, \beta = x, y, z$, which

$$v_x = v_F I \gamma_x, \quad v_y = v_F I \gamma_y, \quad v_z = v_F I \gamma_z, \quad (36)$$

with I the 4×4 identity matrix, and the 4×4 Gamma matrices: $\gamma_x = \sigma_z \otimes i\sigma_y$, $\gamma_y = \sigma_z \otimes i\sigma_x$, $\gamma_z = i\sigma_z \otimes i\sigma_z$. While for the screened interlayer Hubbard repulsion which is rised by the interlayer interaction, is[58, 59]

$$g'_s(\mathbf{k}, \omega) = \frac{g \sinh(d\mathbf{k})}{\sqrt{(\cosh(d\mathbf{k}) + g \sinh(d\mathbf{k}) \Pi(\mathbf{k}, \omega))^2 - 1}}, \quad (37)$$

with the above polarization function can be rewritten as

$$\Pi(\mathbf{k}, \Omega) = -\frac{4}{S} \sum_{\Delta\mathbf{k}} \frac{f_{\mathbf{k}+\Delta\mathbf{k}} - f_{\mathbf{k}}}{E_{\mathbf{k}+\Delta\mathbf{k}} - E_{\mathbf{k}} - \Omega - i\delta}. \quad (38)$$

The polariztion function will becomes ω -independent for the interband transition[60] between the conduction band and valence band which only happen in the strong Coulomb-coupling case in the monolayer silicene[15].

In conclusion, we investigate the manipulation of the phase transition of the semimetal silicene to the Mott insulator (or the paramagnetic Mott insulator in the present of long-range hopping) without applying the magnetic field or the laser beam. There are not nesting at the zero filling for the silicene (see the map-plot in Fig.4), and the AFM order is absent at the begining with $U=0$. That provides the premise for the phase transition from semimetal to insulator. The AFM Mott insulator phase can emerges under the U larger that the critical value expressly for the AB-stacked bilayer silicene or the multilayer bulk one[61], although the silicene is not bipartite like the graphene due to its strong intrinsic SOC except viewed as a composite of two opposite triangular sublattices[62]. In the presence of the on-site Hubbard U in our tight-binding model with the induced layer potential difference, the competing with the spin-dependent exchange field M_s may leads to the topological phase transition between zero and nonzero Chern number[15], and with the tunable Hall current under the bias energy. The charged impurity is proved that affects deeply the DOS of the monolayer and bilayer silicene in this paper, and induced the long-range Coulomb scattering which with the mean elastic diffusion distance $\frac{v_F}{2\Gamma} \sim \sqrt{n}$ in the zero-temperature limit. It's also been found that the increasing of impurity concentration may reduce the critical temperature for the phase transition[63]. and the phase transition to the paramagnetic Mott insulator has been proved to be second order in the decrease of double occupation[45]. The increasing Hubbard U also leads to the renormalization of the kinetic energy or the Fermi velocity in the presence of electron interactions, and even the renormalization quasiparticle mass. We also find that the triplet excitons in the Mott insulator region may arised with the increasing $d_1 + id_2$ pairing instability due to the decreasing of long-range hopping (like the t') which may reduce the inter-sublattice symmetry. The RVB which with the observable charge fluctuation also arised near the critical value for the phase transition of semimetal to insulator (or the paramagnetic silicene to insulator for the case with nonzero NNN hopping). Through the charge impurity scattering together with the Coulomb repulsion, the transport properties (like the optical conductivity) are explored with the different short-range Hubbard interaction in this paper. Finally, in contrast to the AB-stacked bilayer silicene or the multilayer bulk one, the monolayer silicene or the AA-stacked bilayer one have weaker AFM or FM (excitonic) instability and the exchange instability under the large on-site Hubbard U exceeds the critical value. That also related to the SC $d_1 + id_2$ type wave pairing which can be emerged in the bilayer silicene and has the common characteristics of the d -wave SC: like the anisotropic dispersion which also affects the transoprt properties of the charge carriers, and the enhanced particle-hole pairing (like the Cooper pair) strength.

6 Acknowledgement

I thank Peng-Cheng Li for useful discussions.

References

- [1] Feng B, Ding Z, Meng S, et al. Evidence of silicene in honeycomb structures of silicon on Ag (111)[J]. Nano letters, 2012, 12(7): 3507-3511.
- [2] Ezawa M. Valley-polarized metals and quantum anomalous Hall effect in silicene[J]. Physical review letters, 2012, 109(5): 055502.
- [3] Tao L, Cinquanta E, Chiappe D, et al. Silicene field-effect transistors operating at room temperature[J]. Nature nanotechnology, 2015, 10(3): 227.
- [4] Rader O, Varykhalov A, Sanchez-Barriga J, et al. Is There a Rashba Effect in Graphene on 3 d Ferromagnets?[J]. Physical review letters, 2009, 102(5): 057602.
- [5] Liu F, Liu C C, Wu K, et al. d+ i d Chiral Superconductivity in Bilayer Silicene[J]. Physical review letters, 2013, 111(6): 066804.
- [6] Hasegawa Y, Konno R, Nakano H, et al. Zero modes of tight-binding electrons on the honeycomb lattice[J]. Physical Review B, 2006, 74(3): 033413.
- [7] Guzmán-Verri G G, Voon L C L Y. Electronic structure of silicon-based nanostructures[J]. Physical Review B, 2007, 76(7): 075131.
- [8] Guo Z X, Furuya S, Iwata J, et al. Absence and presence of Dirac electrons in silicene on substrates[J]. Physical Review B, 2013, 87(23): 235435.
- [9] Grosso G, Piermarocchi C. Tight-binding model and interactions scaling laws for silicon and germanium[J]. Physical Review B, 1995, 51(23): 16772.
- [10] Min H, Hill J E, Sinitsyn N A, et al. Intrinsic and Rashba spin-orbit interactions in graphene sheets[J]. Physical Review B, 2006, 74(16): 165310.
- [11] Liu C C, Jiang H, Yao Y. Low-energy effective Hamiltonian involving spin-orbit coupling in silicene and two-dimensional germanium and tin[J]. Physical Review B, 2011, 84(19): 195430.
- [12] Liu C X, Qi X L, Zhang H J, et al. Model Hamiltonian for topological insulators[J]. Physical Review B, 2010, 82(4): 045122.
- [13] Yao Y, Ye F, Qi X L, et al. Spin-orbit gap of graphene: First-principles calculations[J]. Physical Review B, 2007, 75(4): 041401.
- [14] Farrell A, Wu P K, Kao Y J, et al. Incommensurate spin density wave as a signature of spin-orbit coupling and precursor of topological superconductivity[J]. Physical Review B, 2016, 94(21): 214424.
- [15] Wu C H. Tight-binding model and ab initio calculation of silicene with strong spin-orbit coupling in low-energy limit[J]. arXiv preprint arXiv:1804.01695, 2018.
- [16] Ezawa M. A topological insulator and helical zero mode in silicene under an inhomogeneous electric field[J]. New Journal of Physics, 2012, 14(3): 033003.
- [17] Ezawa M. Photoinduced topological phase transition and a single Dirac-cone state in silicene[J]. Physical review letters, 2013, 110(2): 026603.
- [18] Ezawa M. Spin valleytronics in silicene: Quantum spin Hall quantum anomalous Hall insulators and single-valley semimetals[J]. Physical Review B, 2013, 87(15): 155415.
- [19] Zhang J, Zhao B, Yang Z. Abundant topological states in silicene with transition metal adatoms[J]. Physical Review B, 2013, 88(16): 165422.
- [20] Guinea F. Spin-orbit coupling in a graphene bilayer and in graphite[J]. New Journal of Physics, 2010, 12(8): 083063.

- [21] Ezawa M, Tanaka Y, Nagaosa N. Topological phase transition without gap closing[J]. Scientific reports, 2013, 3: 2790.
- [22] Ezawa M. Quasi-topological insulator and trigonal warping in gated bilayer silicene[J]. Journal of the Physical Society of Japan, 2012, 81(10): 104713.
- [23] Xiao D, Yao W, Niu Q. Valley-contrasting physics in graphene: magnetic moment and topological transport[J]. Physical Review Letters, 2007, 99(23): 236809.
- [24] Nicol E J, Carbotte J P. Optical conductivity of bilayer graphene with and without an asymmetry gap[J]. Physical Review B, 2008, 77(15): 155409.
- [25] Grimaldi C, Cappelluti E, Marsiglio F. Off-Fermi surface cancellation effects in spin-Hall conductivity of a two-dimensional Rashba electron gas[J]. Physical Review B, 2006, 73(8): 081303.
- [26] Li Z, Marsiglio F, Carbotte J P. Vanishing of interband light absorption in a persistent spin helix state[J]. Scientific reports, 2013, 3: 2828.
- [27] Khveshchenko D V. Ghost excitonic insulator transition in layered graphite[J]. Physical Review Letters, 2001, 87(24): 246802.
- [28] Paolo, Giannozzi, et al. "QUANTUM ESPRESSO: a modular and open-source software project for quantum simulations of materials." J. Phys.: Condens. Matter 21.39 (2009): 395502.
- [29] Perdew J P, Burke K, Ernzerhof M. Generalized gradient approximation made simple[J]. Physical review letters, 1996, 77(18): 3865.
- [30] Nandkishore R, Levitov L S, Chubukov A V. Chiral superconductivity from repulsive interactions in doped graphene[J]. Nature Physics, 2012, 8(2): 158.
- [31] Zhang H, Liu C X, Qi X L, et al. Topological insulators in Bi 2 Se 3, Bi 2 Te 3 and Sb 2 Te 3 with a single Dirac cone on the surface[J]. Nature physics, 2009, 5(6): 438.
- [32] Wu C H. Time Evolution and Thermodynamics for the Nonequilibrium System in Phase-Space[J]. arXiv preprint arXiv:1711.00547, 2017.
- [33] Go A, Millis A J. Spatial Correlations and the Insulating Phase of the High-T c Cuprates: Insights from a Configuration-Interaction-Based Solver for Dynamical Mean Field Theory[J]. Physical review letters, 2015, 114(1): 016402.
- [34] Jafari S A. Dynamical mean field study of the Dirac liquid[J]. The European Physical Journal B, 2009, 68(4): 537-542.
- [35] Li Z, Zhuang J, Chen L, et al. Observation of van HOF singularities in twisted silicene multilayers[J]. ACS central science, 2016, 2(8): 517-521.
- [36] Adam S, Hwang E H, Galitski V M, et al. A self-consistent theory for graphene transport[J]. Proceedings of the National Academy of Sciences, 2007, 104(47): 18392-18397.
- [37] Vargiamidis V, Vasilopoulos P, Hai G Q. Dc and ac transport in silicene[J]. Journal of Physics: Condensed Matter, 2014, 26(34): 345303.
- [38] Wu C, Bernevig B A, Zhang S C. Helical liquid and the edge of quantum spin Hall systems[J]. Physical review letters, 2006, 96(10): 106401.
- [39] Zheng D, Zhang G M, Wu C. Particle-hole symmetry and interaction effects in the Kane-Mele-Hubbard model[J]. Physical Review B, 2011, 84(20): 205121.
- [40] Charbonneau M, Van Vliet K M, Vasilopoulos P. Linear response theory revisited III: Onebody response formulas and generalized Boltzmann equations[J]. Journal of Mathematical Physics, 1982, 23(2): 318-336.
- [41] Dyakonov M I, Perel V I. Current-induced spin orientation of electrons in semiconductors[J]. Physics Letters A, 1971, 35(6): 459-460.
- [42] Haule K, Rosch A, Kroha J, et al. Pseudogaps in an incoherent metal[J]. Physical review letters, 2002, 89(23): 236402.

- [43] Xu W, Haule K, Kotliar G. Hidden Fermi liquid, scattering rate saturation, and Nernst effect: a dynamical mean-field theory perspective[J]. *Physical review letters*, 2013, 111(3): 036401.
- [44] Wang Q H, Lee D H. Quasiparticle scattering interference in high-temperature superconductors[J]. *Physical Review B*, 2003, 67(2): 020511.
- [45] Ebrahimkhas M. Exact diagonalization study of 2D Hubbard model on honeycomb lattice: Semi-metal to insulator transition[J]. *Physics Letters A*, 2011, 375(36): 3223-3227.
- [46] Gebhard F, Girndt A. Comparison of variational approaches for the exactly solvable 1/r-Hubbard chain[J]. *Zeitschrift fr Physik B Condensed Matter*, 1994, 93(4): 455-463.
- [47] Santoro G, Airoldi M, Sorella S, et al. Hubbard model on the infinite-dimensional diamond lattice[J]. *Physical Review B*, 1993, 47(24): 16216.
- [48] Hsu Y F, Guo G Y. Anomalous integer quantum Hall effect in A A-stacked bilayer graphene[J]. *Physical Review B*, 2010, 82(16): 165404.
- [49] Mousavi H. Optical Conductivity of Graphene Sheet Including Electron-Phonon Interaction[J]. *Communications in Theoretical Physics*, 2012, 57(3): 482.
- [50] Sorella S, Tosatti E. Semi-metal-insulator transition of the Hubbard model in the honeycomb lattice[J]. *EPL (Europhysics Letters)*, 1992, 19(8): 699.
- [51] Baskaran G. Impurity band Mott insulators: a new route to high Tc superconductivity[J]. *Science and technology of advanced materials*, 2009, 9(4): 044104.
- [52] Jakli J, Prelovek P. Finite-temperature properties of doped antiferromagnets[J]. *Advances in Physics*, 2000, 49(1): 1-92.
- [53] Havener R W, Liang Y, Brown L, et al. Van hove singularities and excitonic effects in the optical conductivity of twisted bilayer graphene[J]. *Nano letters*, 2014, 14(6): 3353-3357.
- [54] Guinea F, Neto A H C, Peres N M R. Interaction effects in single layer and multi-layer graphene[J]. *The European Physical Journal Special Topics*, 2007, 148(1): 117-125.
- [55] Nair R R, Blake P, Grigorenko A N, et al. Fine structure constant defines visual transparency of graphene[J]. *Science*, 2008, 320(5881): 1308-1308.
- [56] Matthes L, Pulci O, Bechstedt F. Massive Dirac quasiparticles in the optical absorbance of graphene, silicene, germanene, and tinene[J]. *Journal of Physics: Condensed Matter*, 2013, 25(39): 395305.
- [57] Gusynin V P, Sharapov S G. Transport of Dirac quasiparticles in graphene: Hall and optical conductivities[J]. *Physical Review B*, 2006, 73(24): 245411.
- [58] Gonzalez J, Guinea F, Vozmediano M A H. Unconventional quasiparticle lifetime in graphite[J]. *Physical review letters*, 1996, 77(17): 3589.
- [59] Baskaran G, Jafari S A. Gapless spin-1 neutral collective mode branch for graphite[J]. *Physical review letters*, 2002, 89(1): 016402.
- [60] Hwang E H, Sarma S D. Screening, Kohn anomaly, Friedel oscillation, and RKKY interaction in bilayer graphene[J]. *Physical review letters*, 2008, 101(15): 156802.
- [61] Harigaya K. The mechanism of magnetism in stacked nanographite: theoretical study[J]. *Journal of Physics: Condensed Matter*, 2001, 13(6): 1295.
- [62] Sahin H, Peeters F M. Adsorption of alkali, alkaline-earth, and 3 d transition metal atoms on silicene[J]. *Physical Review B*, 2013, 87(8): 085423.
- [63] Iye Y. Magnetic fieldinduced metalinsulator transitions in graphite and diluted magnetic semiconductors[J]. *Philosophical Transactions of the Royal Society of London A: Mathematical, Physical and Engineering Sciences*, 1998, 356(1735): 157-172.
- [64] Bena C, Kivelson S A. Quasiparticle scattering and local density of states in graphite[J]. *Physical Review B*, 2005, 72(12): 125432.

- [65] Tabert C J, Nicol E J. Dynamical conductivity of AA-stacked bilayer graphene[J]. Physical Review B, 2012, 86(7): 075439.
- [66] Kamal C, Chakrabarti A, Banerjee A, et al. Silicene beyond mono-layers different stacking configurations and their properties[J]. Journal of Physics: Condensed Matter, 2013, 25(8): 085508.

Fig.1

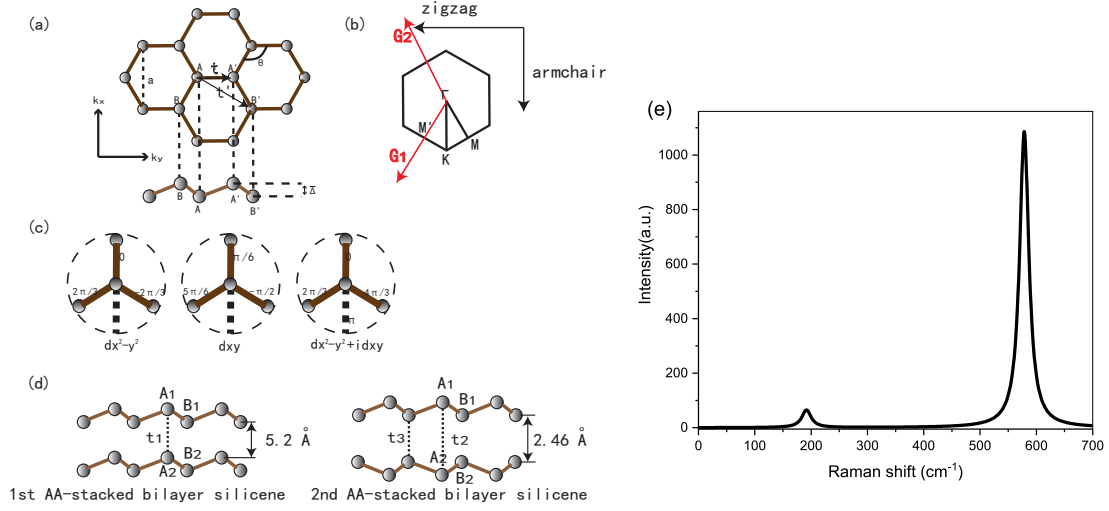


Figure 1: (a) Top view and side view of the silicene. with four sites (sublattices) A, B, A', B' in unit cell. The bond-angle θ and the buckling distance Δ were marked. The three dashed lines with t, t', t'' denotes the nearest-, second nearest-, and third nearest-neighbor hopping, respectively. The blue and green solid lines denotes the hopping in r direction and r' direction respectively, where r' contains the three hopping directions which given by the phase ϕ and r contains the three ones which not given by the phase ϕ . (b) Brillouin zone (the k -space) with the high symmetry points. The Red vector in the right panel is the reciprocal lattice vector $\mathbf{G}_1 = \left(-\frac{2\sqrt{3}\pi}{3a}, -\frac{2\pi}{a}\right)$, $\mathbf{G}_2 = \left(-\frac{2\sqrt{3}\pi}{3a}, \frac{2\pi}{a}\right)$. (c) Phase of the $d_{x^2-y^2}$, d_{xy} , $d_{x^2-y^2} + id_{xy}$ pairing symmetries (left to right) of silicene in real space. (d) the two kinds of the AA-stacked silicene: the first one with the nearest layer distance as 5.2 \AA and intra-layer bond length 2.28 \AA and with bulked distance $\bar{\Delta} = 0.46 \text{ \AA}$ the same as the monolayer one, the second one with the nearest layer distance as 2.46 \AA and intra-layer bond length 2.32 \AA and with lattice constant $a = 3.88$, and the bulked distance becomes $\bar{\Delta} = 0.64 \text{ \AA}$ The interlayer hopping label in the figure are $t_3 \simeq 2 \text{ eV} > t_2 > t_3$. (e) The Lorentzian fit of the Raman spectrum of monolayer silicene.

Fig.2

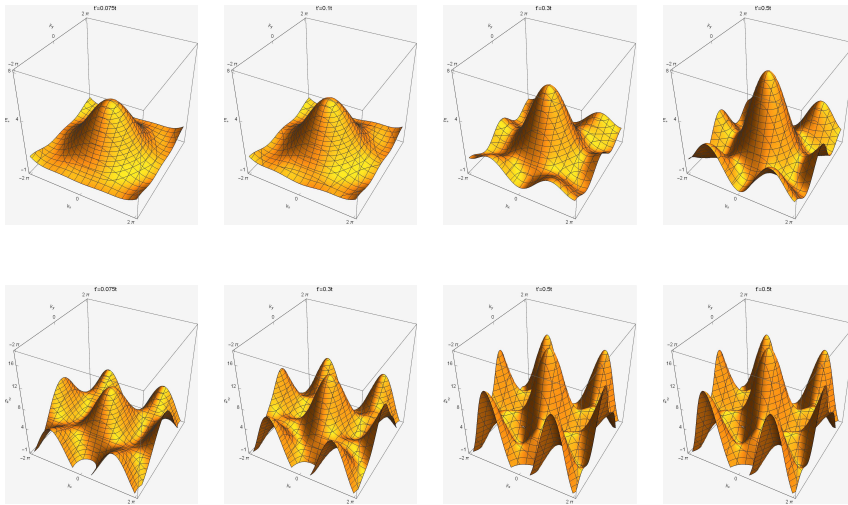


Figure 2: (Color online) 3D Schematic diagram of the band structures of monolayer silicene in momentum space obtained from Eq.(2) and Eq.(3), respectively. The upper panel is the upper bands energy and lower panel the energy in the single-particle picture with different t' . The on-site energy is setted as 1 here and the NN hopping is setted as 1 for simplify. The NNN hopping are $t' = 0.075t$, $t' = 0.1t$, $t' = 0.3t$, $t' = 0.5t$ from left to right.

Fig.3

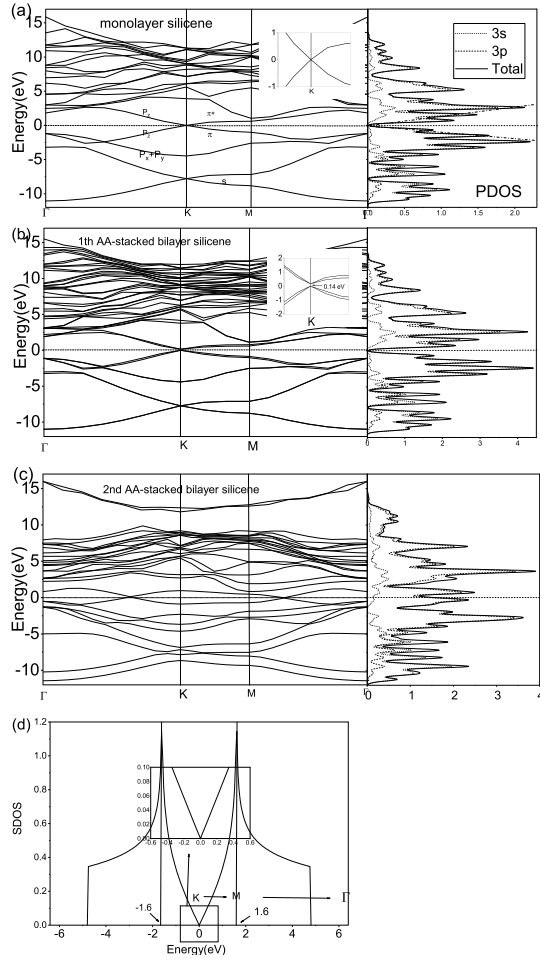


Figure 3: Band structure of the monolayer silicene (a), 1st AA-stacked bilayer silicene (b), and 2nd AA-stacked bilayer silicene (c) as well as their PDOS in the right side. The insets show the enlarged views of band structure in the K-point, which for the bilayer 1st AA-stacked one exhibits a gap as 0.14 eV in the K-point (and the gap 0.15 eV is obtained by using the method of local-density approximation (LDA)), while it's gapless for the monolayer one. There's a slight difference for our results about the 1st AA-stacked silicene from the Ref.[5]s', which exhibit a band crossing as 0.2 eV much smaller than that of the bilayer graphene which is $2t_{\text{inter}}$ [65]. That may due to the different inter-layer separations of the sample, e.g., see Ref.[66]. In (c), the band structure of 2nd AA-stacked silicene exhibit two cross-point in the range of $\Gamma - K$ and $\Gamma - M$, respectively. The π^* -band and π -band which are cross in the Dirac-point are labeled in (a), and the bands main contributed by p_z , $p_x + p_y$, and s orbit are also labeled. From the PDOS, we can clearly see that the silicene is a 3p-orbital-based materials, but the 3s-orbit is dominate below the -5 eV due to its large electronegativity. The PDOS in (a) is similar to the figure of the single-particle DOS (d) which consider only the NN-hopping here. The two Van-Hove singularities emerge at $\varepsilon = \pm 1.6$ eV, which corresponds to the hexagon Fermi surface (nexted) enclosed by the six M-point (the saddle points of the band structure in first BZ) of the as labeled in the figure (see also the Fig.2), while for the case with impurities or the lattice defects, the zero-energy point (neutrality point) exhibits a smeared δ -function with a finite width[64, ?]), They both has a linear dispersion near the neutrality point (see the inset of (c) and the dash-dot line in the right-side of (a)).

Fig.4 caption:(Color online) Map plots (equal value contours) of the tight-binding energy dispersion (upper panel) and their corresponding DOS (bottom panel) for the silicene with particle-hole symmetry where we ignore the broken of inversion symmetry by the bulked structure and the Rashba-coupling (NNN) and consider only the NN hopping. The DOS-map are obtained by the renormalization group method in momentum space. In (a) and (b), we consider the dispersion in hexagonal BZ with the contribution from $t = 1.6$ eV and $t = V_{pp\pi}^{(1)}$ (which measured as -0.72 in Ref.[7] and -1.12 in Ref.[11]) respectively, while in (c) we consider the dispersion in square BZ with $t = 1.6$ eV and with Dirac mass $m_D = 0.32$ eV. The distribution of the DOS is the same as the one shown in Fig.1(d), i.e., arrives the maximum value in the hexagonal Fermi surface where the Fermi surface is nested now. For the case of $t = -0.72$, we can't find the nested hexagonal Fermi surface anymore. Note that we only takes the real part for the computing results.

Fig.5

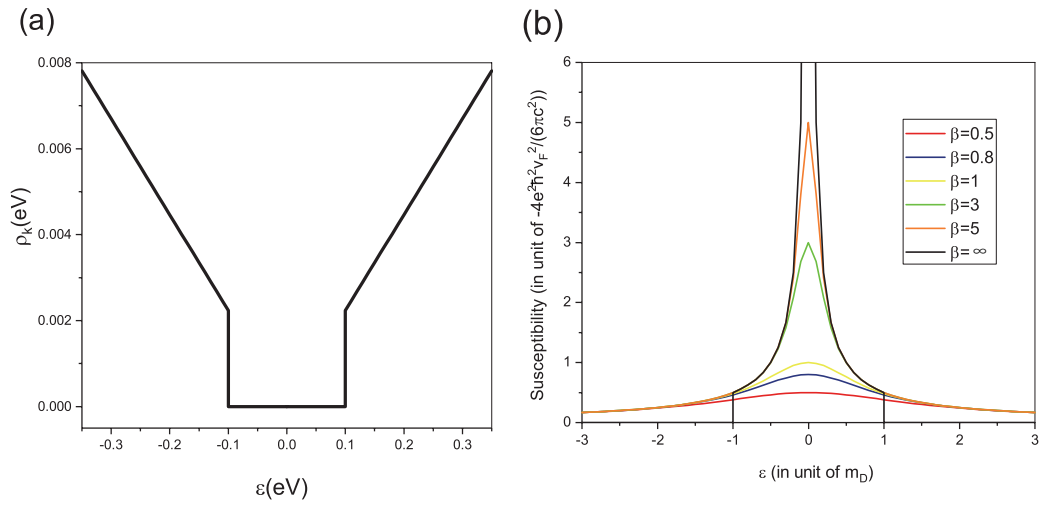


Figure 4: (Color online) (a) DOS at zero temperature as a function of the energy where we set $|\lambda_{SOC} + M| = 0.1$ eV, $R = 0$, $E_{\perp} = 0$. (b) The negative orbital susceptibility as a function of the energy in unit of m_D under the zero-temperature limit $\beta \rightarrow \infty$ and a series of finite temperatures.

Fig.6

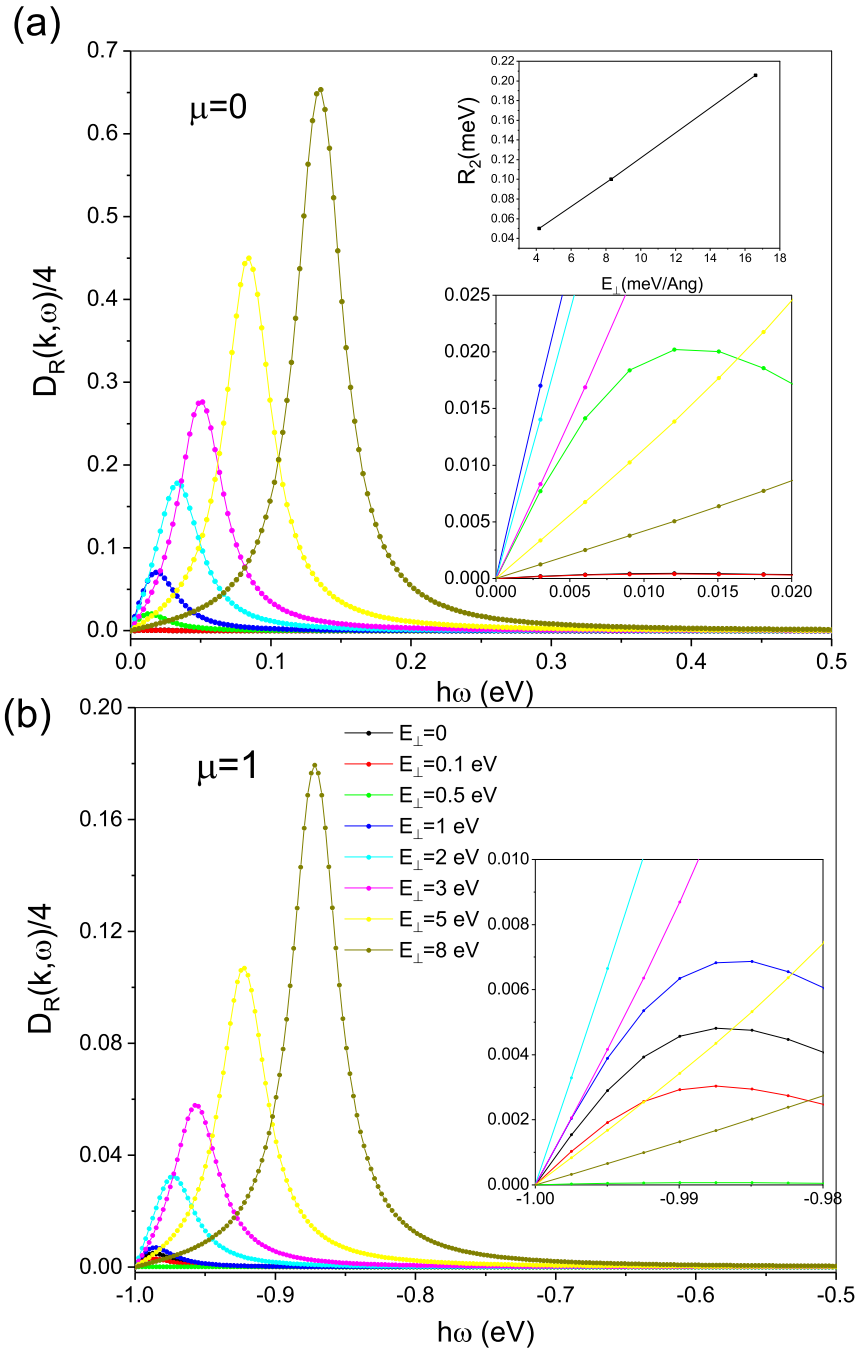


Figure 5: (Color online) The DOS contributed by the Rashba-coupling under different perpendicular electric field strength. The temperature $k_B T$ is set as 0.025 eV and the chemical potential is zero (a) and 1 (b), respectively. When the electric field is zero, there exist only the NNN intrinsic Rashba-coupling; when the electric field was applied, the induced NN Rashba-coupling $R_2(E_{\perp})$ is follow the linear relation with the strength of the applied electric field, $R_2(E_{\perp}) = 0.012E_{\perp}$, as shown in the upper inset. Note that we simplify the Γ as 0.01 in the computational process of this figure.

Fig.7

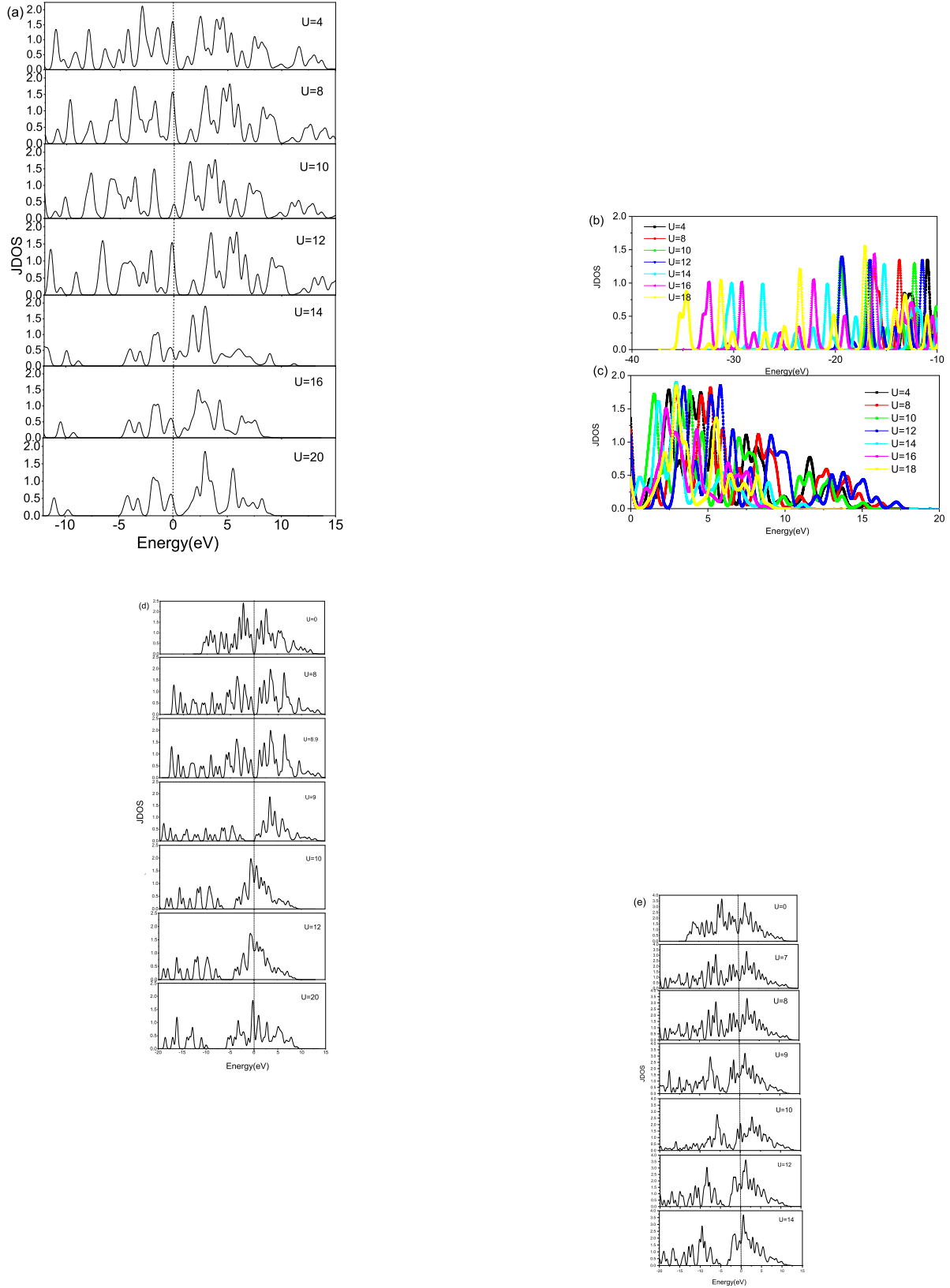


Figure 6: (Color online)(a) Joint DOS (JDOS) of monolayer silicene with the impurity whose strength is 4 eV under different Hubbard U . The value of Hubbard U are labeled in the plot. The zero-energy level are labeled by the dot-line. Note that the silicene here is in AFM order. (b) and (c) shows the JDOS (a) in positive-energy-region and negative-energy-region, respectively. For the pure monolayer silicene (d) and the pure 2nd AA-stacked bilayer silicene (e), we show the resulting JDOS around the critical U .

Fig.8

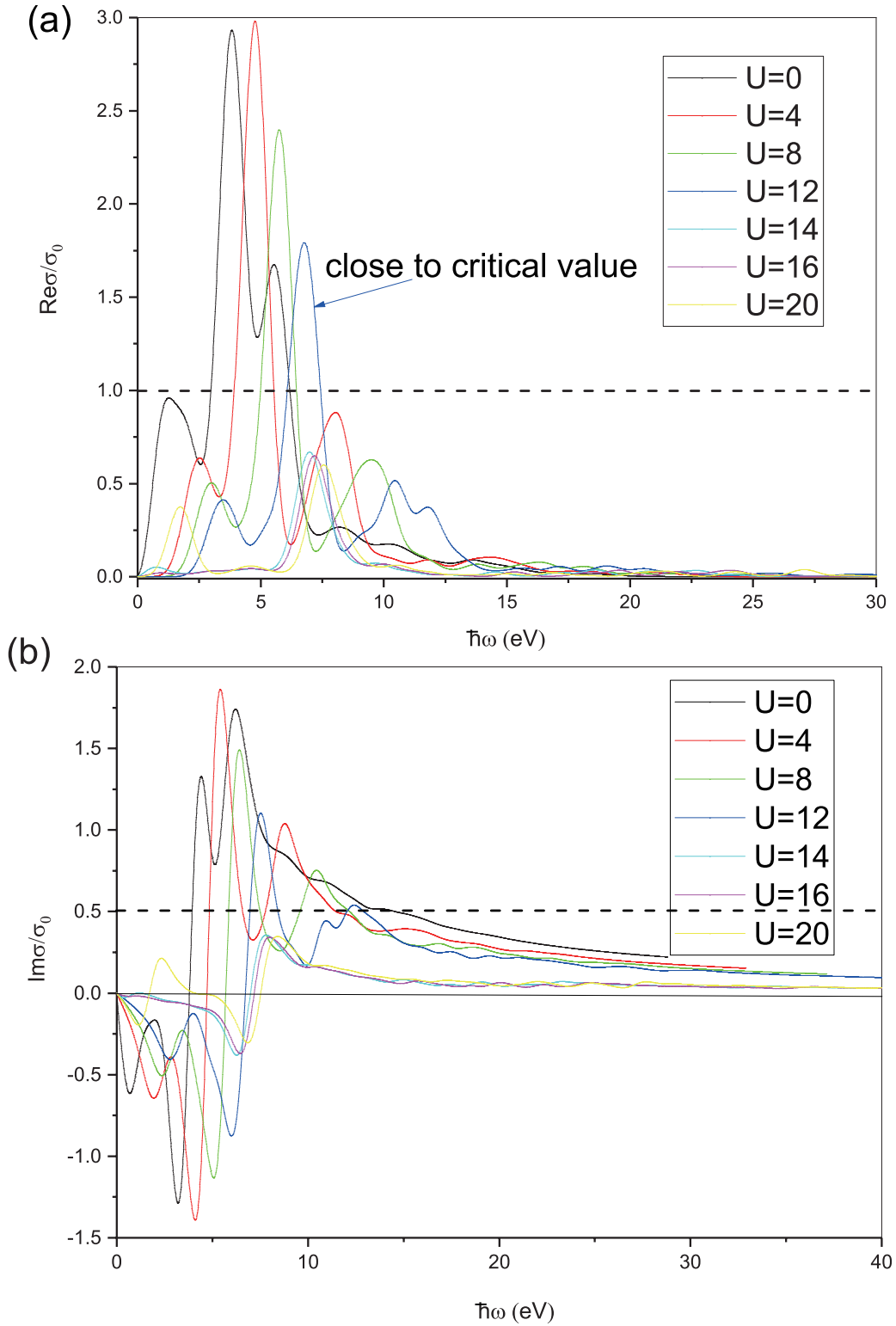


Figure 7: (Color online) Real part (a) and imaginary part (b) of the optical conductivity of the dirty monolayer silicene with the impurity strength 4 eV (corresponds to Fig.7(a)-(c)) under different Hubbard U . The vertical-axis is in unit of ac constant conductivity $\sigma_0 = e^2/(4\hbar)$, which is valid for all the group-IV monolayer honeycomb crystals, and $\sigma_0 = e^2/(2\hbar)$ for the bilayer one.